ANNUAL REVIEWS

Annual Review of Nuclear and Particle Science

Neutron Stars and the Nuclear Matter Equation of State

J.M. Lattimer

Department of Physics and Astronomy, Stony Brook University, Stony Brook, New York 11794-3800, USA; email: james.lattimer@stonybrook.edu

ANNUAL REVIEWS CONNECT

www.annualreviews.org

- Download figures
- Navigate cited references
- Keyword search
- Explore related articles
- Share via email or social media

OPEN ACCESS CC BY

Keywords

neutron stars, dense matter equation of state, neutron matter, gravitational radiation, pulsars

Abstract

Neutron stars provide a window into the properties of dense nuclear matter. Several recent observational and theoretical developments provide powerful constraints on their structure and internal composition. Among these are the first observed binary neutron star merger, GW170817, whose gravitational radiation was accompanied by electromagnetic radiation from a short γ-ray burst and an optical afterglow believed to be due to the radioactive decay of newly minted heavy r-process nuclei. These observations give important constraints on the radii of typical neutron stars and on the upper limit to the neutron star maximum mass and complement recent pulsar observations that established a lower limit. Pulse-profile observations by the Neutron Star Interior Composition Explorer (NICER) X-ray telescope provide an independent, consistent measure of the neutron star radius. Theoretical many-body studies of neutron matter reinforce these estimates of neutron star radii. Studies using parameterized dense matter equations of state (EOSs) reveal several EOS-independent relations connecting global neutron star properties.

Contents

1. INTRODUCTION

Neutron stars offer a unique window into the properties of dense matter. They are born in the aftermath of gravitational-collapse supernovae at the ends of the lives of stars that were initially more massive than about $5M_\odot$ (1). Most stellar mass is lost in stellar winds during a star's later burning phases or expelled by the supernova shock created when the collapsing core reaches nuclear densities and nuclear interactions become strongly repulsive. Initially, a proto–neutron star is lepton-rich with an electron fraction of about 0.35 and a ν_e fraction of about 0.05. Neutrinos are briefly trapped because of the core's high density and opacity, but they diffuse outward over several seconds and leave behind the bulk of their degeneracy energies as heat. In turn, this heat is converted into multiple generations of escaping neutrinos and antineutrinos of all flavors. About 99% of the available neutron star binding energy, approximately 3×10^{53} erg, is radiated in neutrinos with typical energies of 10 to 20 MeV (2). This scenario was nicely confirmed by the detection of about 20 neutrinos over an approximately 10-s interval from SN 1987A by the Kamiokande (3) and IMB (4) neutrino detectors on February 23, 1987.

A neutron star's core efficiently cools, and within minutes thermal effects cease to be important in determining its structure and, with the exception of superfluidity, its composition. The composition is fixed by weak-interaction (i.e., β) equilibrium, which dictates that the neutron, proton, and electron chemical potentials satisfy $\mu_n - \mu_p = \mu_e$.[1] One can identify five important regions in a neutron star: the atmosphere, envelope, crust, and outer and inner cores. The atmosphere, a thin layer (thickness of a few centimeters) with a maximum density of about $\rho \simeq 1$ g cm^{-3}, controls the shape of the observable X-ray spectrum of stars less than a few million years old. The envelope is about 10–100 m thick and extends to $\rho \sim 10^{10}$–10^{11} g cm^{-3}; it is important because its

---

[1]For simplicity, μ_n and μ_p are measured relative to the nucleon mass m_B throughout this review.

composition controls the heat flow into the atmosphere (5). Stars with heavy element envelopes are about five times cooler than those dominated by light elements such as H, He, C, and O, which have larger thermal conductivities. At greater densities within the neutron star crust, nuclei become increasingly neutron-rich. For $\rho \gtrsim 4 \times 10^{11}$ g cm^{-3}, $\mu_n > 0$, and some neutrons become unbound from nuclei (6). In the densest part of the crust, $\rho_s/4 \lesssim \rho_s/2$, where $\rho_s \simeq 2.7 \times 10^{14}$ g cm^{-3} ($n_s = 0.16$ fm^{-3}) is the nuclear saturation density, nuclei become strongly deformed and form a pasta phase (7); the extent of this region varies with the nucleon–nucleon potential, but a comparison of models indicates that on average 60% of the crust's mass is pasta (8). A phase transition to homogeneous nuclear matter occurs at the boundary with the outer core near $\rho_s/2$, where the proton fraction has decreased to about 0.02–0.04.

Because homogeneous nucleonic matter may persist to the star's center, it is unknown whether there is an actual boundary between the inner and outer cores. Generally, the proton fraction increases with density in the star's core, reversing the trend within the star's crust. Various exotic compositions have been predicted for the inner core: hyperons, condensed kaons, or pions in addition to nucleons, or deconfined quark matter in a pure phase or a mixed phase with hadrons. Based on lattice quantum chromodynamics (QCD) calculations, it is expected that matter at very high densities consists of asymptotically free quark matter, but since these calculations (9) are valid only at densities larger than about $40\rho_s$, and the maximum density in a neutron star is less than about $10\rho_s$ (10), it is not clear whether such a phase exists in neutron star interiors. The joint constraints of causality and the observed minimum value of the neutron star maximum mass, $M_{\max} \gtrsim 2M_\odot$, together with new constraints from observations and theory that suggest neutron star radii $R < 13.5$ km (Section 4), tightly constrain the parameters of quark models to narrow regions (11). The high densities of matter surrounding the core quench observable effects of deconfinement except possibly in a star's thermal evolution or dynamical situations such as neutron star mergers, where tidal resonances or fundamental oscillation modes might bear signatures (12). At present, however, no significant observational evidence favors the presence of exotic matter in the inner core.

Neutron star masses, radii, moments of inertia, binding energies, tidal deformabilities, and oscillation frequencies are potentially measurable. Their calculation requires knowledge of only the total energy density ε and pressure P as functions of baryon density n_B. Laboratory nuclei provide important details of the equation of state (EOS) up to ρ_s, and heavy-ion collisions add some constraints for densities up to about $5\rho_s$, but only for hot, nearly symmetric nuclear matter (SNM). Neutron star matter, by contrast, is cold and extremely neutron-rich with proton fractions of order a few percent near ρ_s, so a considerable extrapolation from hot, symmetric matter is required. Fortunately, experiments involving systems close to unitarity (13) and theoretical calculations of pure neutron matter (PNM) may provide a substantial base on which to build neutron star models, as discussed in Section 2.

Other aspects of neutron stars, most importantly their thermal evolution, probe compositional details. The faster-than-expected real-time cooling (14) of the 330-year-old neutron star in the Cassiopeia A supernova remnant hints at the onset of neutron superfluidity in the star's core (15, 16). At least 20 neutron stars have measured temperatures and known or estimated ages, and these data enable comparison with neutron star thermal evolution calculations. The inferred luminosity of the possible neutron star (17, 18) in the remnant of SN 1987A suggests that its envelope consists largely of light nuclei rather than heavier elements of the iron peak that would represent the lowest energy state at those densities. But the largest effect that composition has on neutron star cooling is the presence or absence of nucleon direct Urca neutrino cooling (19, 20) in the star's core, which requires a minimum proton fraction of 1/9. This process is about 10^6 times more efficient than the modified Urca process that otherwise dominates. Since the proton fraction likely increases with density in the neutron star core, massive stars that exceed the

proton fraction threshold cool rapidly—possibly below the level of detectability, depending on details of superfluidity in the star's core—within about a hundred years. The available evidence suggests (5) that rapid cooling does not occur in most stars. Nevertheless, there are several known core-collapse supernova remnants without detected neutron stars that could be examples of rapid cooling, unless their neutron stars all collapsed into black holes because of fallback accretion. This could be possible if they had relatively large masses.

Prior reviews (21, 22) have summarized several aspects of neutron stars that are not repeated here. These include a detailed discussion of constraints established from causality and the largest accurately measured pulsar mass, details of pulsar-timing mass measurements, and synopses of mass and radius estimates from X-ray observations of quiescent and isolated neutron stars as well as from photospheric radius expansion bursts. References 21 and 22 also explore how measurements of nuclear properties and nuclear collisions constrain the nuclear symmetry energy and its strong role in determining the neutron star radius. There have been additional advances, including the discovery of a few more massive pulsars near $2M_\odot$ [those with mass uncertainties less than $0.2M_\odot$ include PSR J0348+0432 with $2.01 \pm 0.04M_\odot$ (23), PSR J2215+5135 with $2.23^{+0.17}_{-0.15}M_\odot$ (24), and PSR J0740+6620 with $2.08 \pm 0.07M_\odot$ (25)] and the development of the cooling tail model, which offers improvements in the modeling of quiescent X-ray sources (26, 27), but this review focuses on other progress.

The main topics in this review include the following.

- Advances have been made in many-body theory relevant to the EOS of PNM (Section 2), which is closely related to neutron star matter, and in measurements of the neutron skins of neutron-rich nuclei. These advances offer new insights into the nuclear symmetry energy and, therefore, into neutron star radii and tidal deformabilities.
- Novel parameterizations of the EOS of high-density matter have proved to be powerful tools in inferring bounds for neutron star properties (Section 3). They have also revealed new or have refined known semiuniversal (i.e., EOS-insensitive) relations connecting global neutron star properties, such as masses, radii, moments of inertia, binding energies, and tidal deformabilities.
- Gravitational wave (GW) observations of the binary neutron star (BNS) merger GW170817 (28) provide new constraints on the radii of typical ($1.4M_\odot$) stars via measurements of their tidal deformabilities (Section 4). The nearly simultaneous electromagnetic (EM) observations of an associated short γ-ray burst and kilonova also offer evidence of an upper limit to $M_{max} \lesssim 2.3M_\odot$ (29), which complements the lower limit of $M_{max} \gtrsim 2M_\odot$ from the most massive accurately measured pulsars. In addition, observations of other BNS and black hole–neutron star (BHNS) mergers have possible ramifications regarding our knowledge of neutron star properties.
- X-ray pulse-profile measurements of the rapidly rotating pulsars PSR J0030+0451 (30, 31) and PSR J0740+6620 (32, 33) with data acquired with the Neutron Star Interior Composition Explorer (NICER) space telescope have led to independent mass and radius estimates (Section 5).

2. THE IMPORTANCE OF NEUTRON MATTER

The PNM EOS is significant for two reasons. First, it establishes strong constraints on the nuclear symmetry energy, and second, it closely approximates the neutron star EOS from densities of about $n_s/2$, where the heterogeneous crust containing nuclei makes the transition to homogeneous nucleon matter, up to 2–$3n_s$ or even higher, where hyperons, a kaon or pion condensate, or quark matter might appear. There are two ways to define the nuclear symmetry energy: It can be viewed

as the difference $S(n_B)$ between the energies of PNM and SNM at a given density, or it can be related to the lowest-order coefficient $S_2(n_B)$ in a Taylor expansion of the energy in the neutron excess $1 - 2x$:

$$S(n_B) = E_B(n_B, 0) - E_B(n_B, 1/2), \qquad S_2(n_B) = \frac{1}{8} \frac{\partial^2 E_B(n_B, x)}{\partial x^2}. \qquad 1.$$

Studies indicate that higher-order terms in the expansion are relatively small (contributing $\lesssim 1$–2 MeV around n_s) (34–36). We can take the symmetry energy to be S, so

$$E_B(n_B, x) \simeq E_B(n_B, 1/2) + S(n_B)(1 - 2x)^2 \simeq E_B(n_B, 0) - 4S(n_B)x(1 - x). \qquad 2.$$

In a neutron star, matter is in β equilibrium since weak-interaction timescales are negligible except in dynamical environments, so matter can be considered to be catalyzed in the lowest energy state. The β-equilibrium proton fraction x is determined by

$$\frac{\partial [E(n_B, x) + E_\ell]}{\partial x} = \mu_p - \mu_n = \mu_e = \mu_\mu, \qquad 3.$$

where E_ℓ is the lepton energy per baryon.[2] Throughout the bulk of the crust and core, electrons are relativistic and degenerate. At n_s, $x \simeq 0.04$. The usual nuclear symmetry energy parameters S_V and L are related to PNM properties:

$$S_V \equiv S_2(n_s) \simeq E_{\mathrm{PNM}}(n_s) + B, \qquad L \equiv 3n_s \left[\frac{\mathrm{d}S_2(n_B)}{\mathrm{d}n_B} \right]_{n_s} \simeq \frac{3P_{\mathrm{PNM}}(n_s)}{n_s}, \qquad 4.$$

where E_{PNM} and P_{PNM} are the PNM energy and pressure, respectively, and $B \equiv -E_B(n_s, 1/2) \simeq 16$ MeV is the bulk binding energy at saturation.

2.1. Chiral Effective Field Theory

During the past few years, there has been a revolution in the understanding of dense nuclear matter, whose constituents—neutrons and protons—have a complex substructure. Their interactions have presented a challenge in nuclear theory for almost a century. The development of chiral effective field theory (χEFT) (37, 38) now provides the only known framework that allows a systematic expansion of nuclear forces at low energies (39–42) based on the symmetries of QCD, the fundamental theory of the strong interaction. In particular, χEFT allows one to derive systematic estimates of uncertainties for thermodynamic quantities. As for any effective low-energy theory, χEFT contains an intrinsic breakdown scale, $\Lambda_b \approx 600$ MeV, which is a characteristic momentum scale associated with the interactions at short distances; when the relative momentum between nucleons is small compared with it, χEFT aims to provide a model-independent, systematically improvable description of nuclear interactions and observables. When approaching Λ_b with increasing energy or density, the convergence of the effective expansion breaks down.

Recently, a novel framework for quantifying correlated effective field theory (EFT) truncation errors has been developed (43–46) for zero-temperature matter with two- and three-nucleon interactions up to next-to-next-to-next-to-leading order (N³LO). For details, readers are referred to the companion article by Drischler et al. (47) in this volume. Progress has been such that reliable calculations now exist up to about $2n_s$ (**Figure 1**). EFT truncation errors dominate the theoretical uncertainty, which, in the pressure, is about $\pm 25\%$ at $2n_s$ but only about 10% at n_s. Statistical analysis indicates that the EOS is strongly correlated; correlation lengths are comparable to the

---

[2] Muons are present if $\mu_e > m_\mu c^2 \simeq 105.66$ MeV.
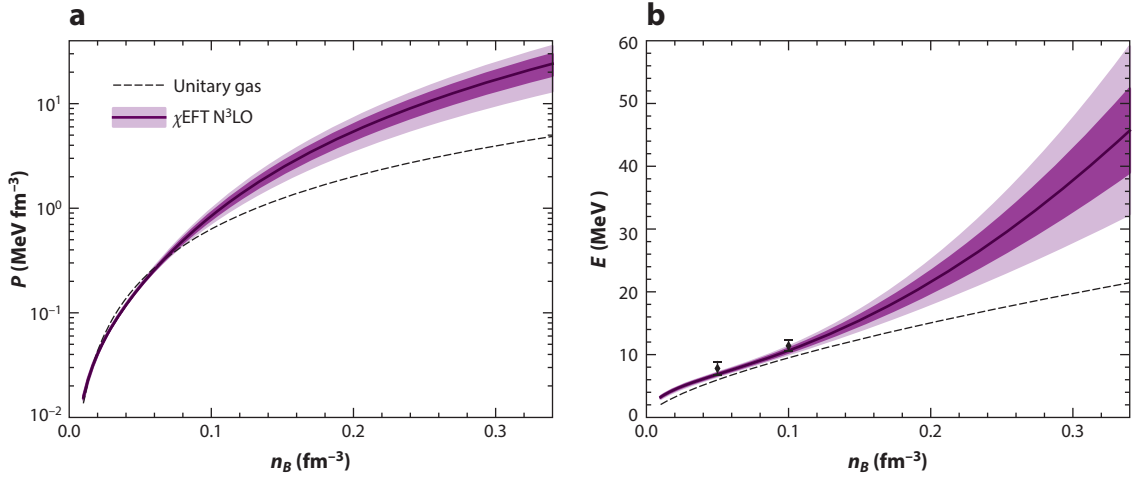
Figure 1

(*a*) P_{PNM} and (*b*) E_{PNM} from χEFT studies, with $\pm 1\sigma$ uncertainties indicated by dark shading and $\pm 2\sigma$ uncertainties indicated by light shading. Corresponding quantities for a unitary gas are shown for comparison. The energies established from doubly magic nuclei (48) at 0.1 fm^{-3} and from the electric dipole polarizability of ^{208}Pb at 0.05 fm^{-3} (49) are indicated in panel *b* with data points with $\pm 1\sigma$ uncertainties. Abbreviations: χEFT, chiral effective field theory; N^{3}LO, next-to-next-to-next-to-leading order; PNM, pure neutron matter. Figure adapted from Reference 50.

Fermi wave number, about 1.3 fm, at n_s. Practically speaking, if a specific parameterized contact interaction predicts $E_{PNM}(n_B)$ near the bottom of the uncertainty band, $P_{PNM}(n_B)$ will also be near the bottom of this band; moreover, the energy and pressure will be near the bottom of the band at other densities as well. Without including these correlations, bounds on the symmetry energy, tidal deformabilities, and other quantities derived from the EOS are overestimated.

Neutron star matter requires the energies of matter with finite proton concentrations. χEFT results for matter with arbitrary proton fractions have been calculated (35, 36, 45), but they do not saturate inside the empirical windows for SNM, $n_s \sim 0.15$–0.16 fm^{-3} and $B \sim 15$–17 MeV. Saturation in SNM emerges from a delicate cancellation sensitive to the short- and intermediate-range three-body interactions at next-to-next-to-leading order (NNLO), in contrast to PNM at N^{3}LO, where these interactions are Pauli-blocked (51). Nevertheless, a strong correlation between PNM and SNM is found. Reference 46 used the saturation point from χEFT SNM calculations and then determined S_V and L using Equation 4 with the PNM results (PNM+SNM in **Figure 2**). Alternatively, since χEFT SNM does not saturate inside the empirical window, one can use B and n_s values from the empirical window together with the PNM results (PNM+MC in **Figure 2**). The resulting correlations have different slopes (the latter resembles that inferred by Reference 52), but both methods yield consistent S_V and L values at the 1σ level.

Figure 2 also displays the empirical correlation established from nuclear masses (using $\sigma = 1$ MeV for the arbitrary mass uncertainty defined in Reference 53). The observed correlation is due to the competition between surface and volume symmetry energies, which implies $dS_S/dS_V \sim <I^4 A^2>/<I^4 A^{5/3}> \sim 6$ (54), where the angled brackets indicate an average over heavy nuclei with mass A and neutron excess $IA = N - Z$. The fact that S_S and L are highly correlated leads to an empirical S_V-L correlation with a slope $dL/dS_V \sim 13$. The χEFT estimates of S_V and L agree with those inferred from nuclear masses, although their correlation slopes differ. These slopes do not have to agree since they result from different physical considerations. A related finding is that the ground-state energies of doubly magic nuclei are most highly correlated with the
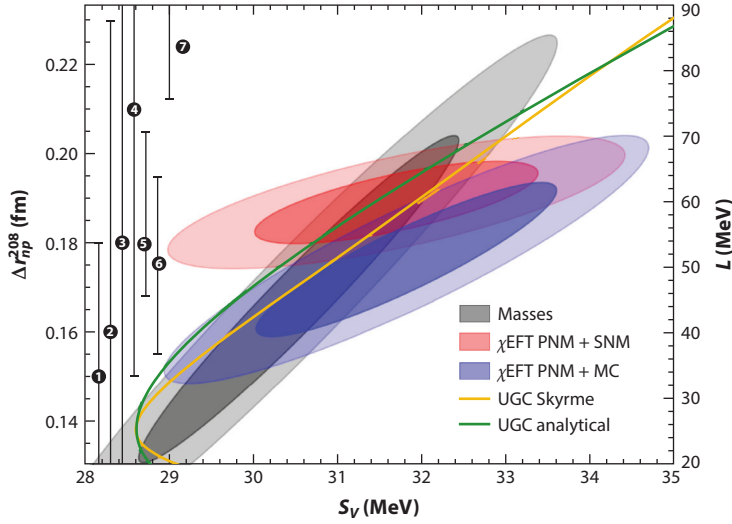
Figure 2

S_V-L correlations from χEFT [*red:* PNM+SNM (46); *blue:* PNM+MC] and nuclear masses [*gray* (53)]. Darker regions show 68% confidence ellipses; lighter regions show 95% confidence ellipses. The dark yellow and green curves represent the UGC from a Skyrme model and from an analytical model (Equation 10), respectively (13). The circled numbers and vertical lines on the left-hand side indicate Δr_{np}^{208} measurements (see **Table 1**) with arbitrary x positions and using Equation 5 to provide the vertical scale relative to L, as follows: (❶) coherent $\pi^0\ \gamma$ production (57), (❷) pion scattering (58), (❸) antiproton annihilation (59, 60), (❹) elastic proton scattering (61), (❺) dispersive optical model (62), (❻) neutron skin thicknesses of Sn isotopes (56), (❼) parity-violating electron scattering (PREX+PREX-II) (63). Abbreviations: χEFT, chiral effective theory; MC, Monte Carlo; PNM, pure neutron matter; SNM, symmetric nuclear matter; UGC, Unitary Gas Conjecture.

symmetry energy at a density $n_1 = 0.1\ \text{fm}^{-3} \sim 2n_s/3$, yielding $S(0.1\ \text{fm}^{-3}) = 25.5 \pm 1.0\ \text{MeV}$ (48), which is equivalent to $E_N(0.1\ \text{fm}^{-3}) = 11.4 \pm 1.0\ \text{MeV}$ and consistent with χEFT (**Figure 1**).

2.2. Neutron Skins, Dipole Polarizabilities, and the Giant Dipole Resonance

The L value can also be inferred from other experiments, including measurements of the neutron skins of neutron-rich nuclei, the dipole polarizability, and the isovector giant dipole resonance. It is often argued that L is linearly correlated with Δr_{np}^{208}, the difference between the root mean square radii of the neutron and proton distributions of ^{208}Pb—as, for example, in the following equation from Reference 55:

$$\Delta r_{np}^{208} = 0.00147(L/\text{MeV}) + (0.101 \pm 0.022)\ \text{fm}. \qquad 5.$$

However, there is an additional significant dependence on S_V (56). Nevertheless, a strong linear correlation (with no S_V contamination) does exist with the symmetry energy slope $\tilde{L} \equiv 3n(\text{d}S/\text{d}n)$ at a density corresponding to the mean density in the nuclear surface, $n_1 \simeq 2n_s/3$ (48). The precise relation depends slightly on the functional dependence of the underlying nuclear interactions used to calibrate it. Measured Δr_{np}^{208} values (**Table 1**) are displayed with uncertainties in **Figure 2**, where the approximate linear relation shown in Equation 5 is used to provide the vertical scale. It is apparent that, at the present time, neutron skin measurements are not sufficiently accurate to place tight constraints on the nuclear symmetry energy properties.

Table 1 Neutron skin measurements of ^{208}Pb with 1σ uncertainties

Experiment	Δr_{np} (fm)	Reference
Coherent π^0 γ production	$0.15^{+0.03}_{-0.04}$	57
Pion scattering	0.16 ± 0.07	58
Antiproton annihilation	0.18 ± 0.06	59, 60
Elastic proton scattering	0.21 ± 0.06	61
Dispersive optical model	$0.18^{+0.25}_{-0.12}$	62
Neutron skin thicknesses of Sn isotopes	0.175 ± 0.020	56
Parity-violating electron scattering (PREX+PREX-II)	0.283 ± 0.071	63

The parity-violating electron scattering experiment PREX (64) is claimed (65) to have theoretical systematic uncertainties that are better understood than those of other methods. Including the data from PREX-II—its recent second run (63), which reduced the original PREX uncertainties by about half—yields $L = 110 \pm 36$ MeV and a corresponding $S_V = 38 \pm 5$ MeV (66). These values of S_V and L are in apparent tension with results from neutron matter theory and most other experimental inferences, but a more detailed analysis (J.M. Lattimer, manuscript in preparation) indicates that this analysis understates the uncertainties of L and S_V such that they, in fact, are consistent at the 68% confidence level with other expectations. Also of great interest is the upcoming CREX measurement of the neutron skin of ^{48}Ca, Δr_{np}^{48}, by parity-violating electron scattering (67), which is expected by the end of 2021. Ab initio calculations with NNLO forces yield 0.12 fm $< \Delta r_{np}^{48} < 0.15$ fm and suggest 47 MeV $< L < 53$ MeV (68).

Another observable shedding light on the symmetry parameters is the electric dipole polarizability, α_D: the ratio of the induced nuclear dipole moment to an applied electric field. The liquid droplet model predicts a nearly linear correlation between $\alpha_D S_V$ and Δr_{np}, which has been confirmed using different nuclear interactions in the case of ^{208}Pb (69):

$$S_V \alpha_D^{208} e^2 = [301 \pm 32 + (1{,}922 \pm 73)\Delta r_{np}^{208}/\text{fm}] \text{ MeV fm}^3. \qquad 6.$$

The experimental value is $\alpha_D^{208} e^2 = 19.6 \pm 0.6$ fm^3 (70). Individual Δr_{np}^{208} measurements thus yield ranges for S_V. For example, for PREX-II, one finds $S_V \simeq 43.1 \pm 7.4$ MeV, which is consistent with the estimate of Reference 66 but not with other nuclear physics expectations. A relation similar to Equation 6 exists for Sn^{120}, for which both α_D and Δr_{np}^{120} have been measured, yielding $S_V \simeq 34.5 \pm 6.7$ MeV, which is consistent with χEFT and nuclear mass inferences. However, in both cases the uncertainties are too large to contribute significant constraints. Reference 49 found that the dipole polarizability of ^{208}Pb is most highly correlated with the symmetry energy at the density $n_2 = 0.05$ fm$^{-3} \sim n_s/3$, and determined $S(n_2) = 16.5 \pm 1.0$ MeV, which is equivalent to $E_N(n_2) \simeq 7.8 \pm 1.2$ MeV, consistent with χEFT (**Figure 1**).

In a similar fashion, the central energy of the giant dipole resonance is most strongly correlated with the symmetry energy at the density n_1 (71). For ^{208}Pb, it is thereby estimated that $S(n_1) = 24.1 \pm 0.8$ MeV, which is equivalent to $E_N(n_1) \simeq 9.9 \pm 1.0$ MeV and consistent with the estimate from Reference 48 and χEFT (**Figure 1**).

2.3. The Unitary Gas

PNM bears an interesting resemblance to the unitary gas (72), a theoretical system of fermions that undergo pairwise s-wave interactions with an infinite scattering length a_s ($|a_s k_F|^{-1} \to 0$) and a vanishing effective range r_{eff} ($r_{\text{eff}} k_F \to 0$), where the Fermi momentum is $k_F = (3\pi^2 n_B)^{1/3}$. Since

the average particle separation is the only length scale of the system, the energy of the unitary gas E_{UG} becomes proportional to the Fermi energy:

$$E_{UG} = \frac{3\hbar^2 k_F^2}{10 m_N}\xi_0 \simeq 12.6\left(\frac{n_B}{n_s}\right)^{2/3} \equiv E_{UG,0}\left(\frac{n_B}{n_s}\right)^{2/3}, \qquad 7.$$

where the Bertsch parameter $\xi_0 \simeq 0.37$ is experimentally measured (73, 74).

For PNM, $|a_s k_F|^{-1} = 0.03(n_B/n_s)^{1/3}$ and $r_{eff}k_F = 4.53(n_B/n_s)^{1/3}$. Thus, the neutron–neutron interaction in the s-wave channel is strongly attractive. Also, the interparticle spacing is much larger than the effective range of the interaction. The system is then fully described by k_F and a_s. Systems with similar values of $a_s k_F$ will experience the same physics. PNM at very low densities, for instance, $n_B \sim 0.01 n_s$, where only s-wave contributions are important, is close to the unitary limit (75). However, at large densities, factors such as effective range effects, interactions in higher-order partial waves, and tensor contributions can become important. Nevertheless, forces with negative scattering lengths at very low densities, or nonzero effective ranges, have higher energies than the unitary gas (76), and this trend continues at higher densities, even if s-wave effective range effects are no longer negligible. In addition, PNM three-body forces, which must be repulsive to fit energy levels of light nuclei in ab initio calculations, more than compensate for small, possibly attractive p- and d-wave interactions, adding at least a few MeV to neutron energies at n_s.

The Unitary Gas Conjecture (UGC) (13) states that $E_{PNM} > E_{UG}$ at all densities relevant for neutron stars. The unitary gas energy and pressure ($P_{UG} = 2n_B E_{UG}/3$) are shown in **Figure 1**; χEFT PNM clearly obeys the UGC. Under the assumption that quadratic interpolation in neutron excess between PNM and SNM is accurate, the UGC constrains the symmetry parameters. E_{PNM} can be expanded around n_s by

$$E_{PNM}(u) = S_V - B + \frac{L}{3}(u-1) + \frac{K_N}{18}(u-1)^2 + \frac{Q_N}{162}(u-1)^3 \cdots, \qquad 8.$$

where $u = n_B/n_s$, K_N is the PNM incompressibility, and Q_N is the PNM skewness. Supposing $E_{PNM} = E_{UG}$ at some density $u_t = n_{Bt}/n_s$, to guarantee $E_{PNM} \geq E_{UG}$ at both lower and higher densities, one demands both $(dE_{PNM}/du)_{u_t} = (dE_{UG}/du)_{u_t}$ and $(d^2 E_{PNM}/du^2)_{u_t} \geq (d^2 E_{UG}/du^2)_{u_t}$. Evaluating these conditions, and ignoring skewness contributions, gives

$$E_{UG,0} u_t^{2/3} \leq S_V - B + \frac{L}{3}(u_t - 1) + \frac{K_N}{18}(u_t - 1)^2,$$

$$2 E_{UG,0} u_t^{2/3} = L u_t + \frac{K_N}{3} u_t(u_t - 1), \qquad K_N \geq -2 E_{UG,0} u_t^{2/3}. \qquad 9.$$

In terms of the parametric variable u_t, these equations define bounds for S_V, L, and K_N obeying the UGC. The first equation shows that, irrespective of the value of K_N, the smallest value of S_V occurs for $u_t = 1$ and is $S_{V,min} = B + E_{UG,0} \simeq 28.6$ MeV. For this value, $L = 2E_{UG,0} = 25.2$ MeV and $K_N \geq -25.2$ MeV. For all other values of u_t, S_V increases, but L increases when $u_t < 1$ and decreases when $u_t > 1$. The allowed region in S_V-L space, which is shown in **Figure 2** using a Skyrme-type nuclear interaction in place of Equation 8, encompasses both χEFT and nuclear mass (53) results. The bound in the S_V-L plane depends only moderately on K_N as well as on the assumed density dependence of E_{PNM}. An analytical estimate is enabled by setting $K_N = 3L$, which is consistent with nuclear systematics (13), and eliminating u_t from the first two equations of Equation 9,

$$S_V = B + \frac{L}{6}\left[1 + 2\left(\frac{2E_{UG,0}}{L}\right)^{3/2}\right], \qquad 10.$$

which is also shown in **Figure 2**. The S_V-L bound is robust because u_t varies over a relatively small range ($0.4 < u_t < 1.2$ in **Figure 2**). It should be noted that the UGC does not guarantee $P_{PNM} > P_{UG}$ at all densities (**Figure 1**).

2.4. Implications for Neutron Star Structure

The most conservative bounds on radii are set jointly by causality and an assumed M_{max} (21). The absolute minimum is set from the maximally compact EOS (77), which has the causal EOS $P = \varepsilon - \varepsilon_m$ for $\varepsilon \geq \varepsilon_m$, and $P = 0$ otherwise. Having a single parameter, ε_m, the Tolman-Oppenheimer-Volkoff structure solutions scale with it or with the assumed M_{max} (**Figure 3a**), where $M_{max} = 4.1(\varepsilon_s/\varepsilon_m)^{1/2} M_\odot$ with $\varepsilon_s = \varepsilon(n_s) \simeq 150$ MeV fm^{-3}. These solutions each represent the minimum possible radius $R_{min}(M)$ for that value of M_{max}.

This EOS is not a good approximation for a hadronic star that contains a crust and therefore has $P > 0$ for densities $\varepsilon < \varepsilon_m$. Ironically, a hadronic EOS (i.e., crust + χEFT) matched to the causal EOS $P = \varepsilon - \varepsilon_m + P_m$ above the matching density $\varepsilon_m = \varepsilon(n_m)$ produces an M-R curve with the largest possible radii R_{max} and the largest possible value of M_{max}. **Figure 3a** shows $R_{max}(M)$ with $\pm 1\sigma$ and $\pm 2\sigma$ χEFT uncertainties assuming $n_m = 2n_s$, which is about the largest value consistent with reasonable and quantifiable uncertainties.
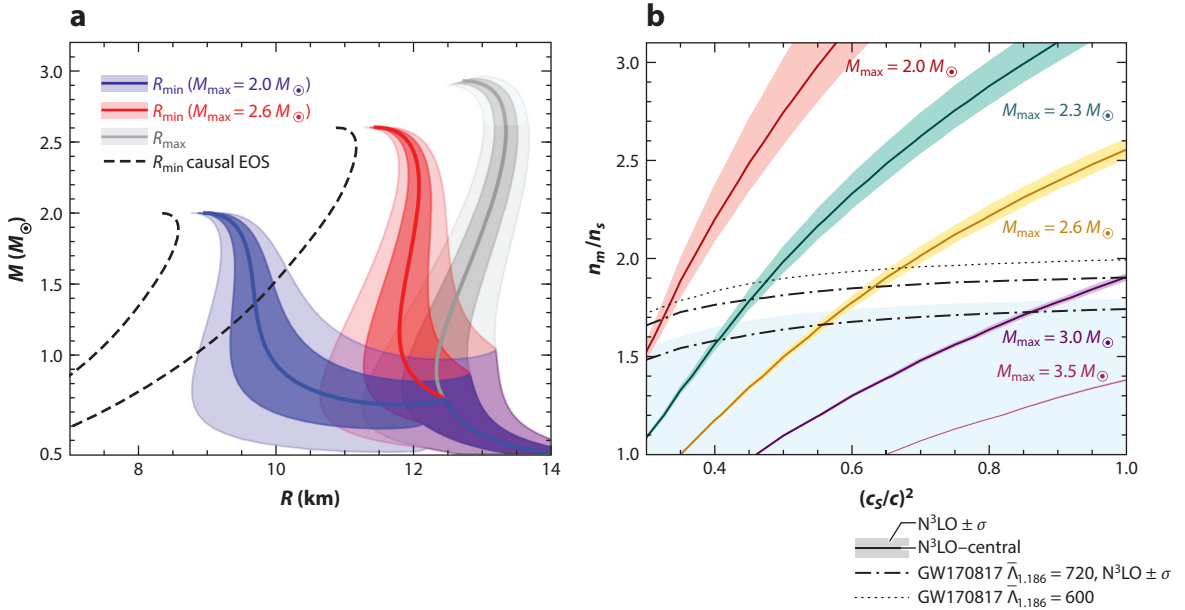
Figure 3

(*a*) Bounds on M-R trajectories. Dashed lines show minimum radii R_{min} based on causality and two assumed values of M_{max} ($2M_\odot$, $2.6M_\odot$). Minimum and maximum R_{max} radii for neutron stars with a crust are determined with the χEFT EOS for $n_m \leq 2n_s$ and causal EOSs for $n_m > 2n_s$ and are indicated by colored bands showing $\pm 1\sigma$ and $\pm 2\sigma$ χEFT uncertainties (see Section 2.4 for computational details). The blue and red bands show R_{min} for $M_{max} = 2M_\odot$ and $2.6M_\odot$, respectively, and the gray bands show R_{max} trajectories. (*b*) Contours of M_{max} along R_{max} trajectories as functions of the matching density n_m and c_s^2, assuming the EOS $P = (c_s/c)^2(\varepsilon - \varepsilon_m) + P_m$ for $\varepsilon > \varepsilon_m$. Dashed–dotted lines show the GW170817 constraint $\bar{\Lambda}_{1.186} = 720$ with $\pm 1\sigma$ χEFT uncertainties. Light blue shading indicates the disallowed region for the central χEFT EOS, and the dotted line indicates the upper 1σ bound if, instead, $\bar{\Lambda}_{1.186} = 600$. Abbreviations: χEFT, chiral effective field theory; EOS, equation of state; N^{3}LO, next-to-next-to-next-to-leading order. Figure adapted from Reference 50.
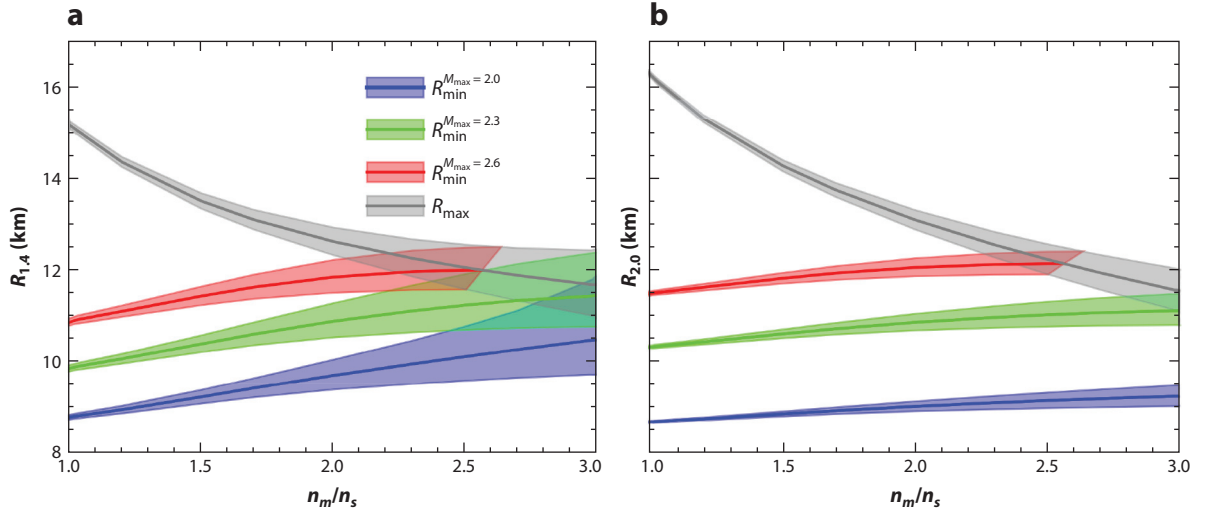
Figure 4

Minimum and maximum radii as functions of matching density n_m for assorted values of $M_{\max}$ for (*a*) $1.4M_\odot$ and (*b*) $2.0M_\odot$ stars. Bands represent $\pm 1\sigma$ chiral effective field theory uncertainties. Figure adapted from Reference 50.

Realistic minimum radii, by contrast, are obtained by introducing an energy density discontinuity $\Delta\varepsilon$ at ε_m. Above the density $\varepsilon_m + \Delta\varepsilon$, the EOS is again taken to be causal, $P = \varepsilon - \varepsilon_m - \Delta\varepsilon + P_m$. Increasing $\Delta\varepsilon$ reduces $M_{\max}$ and increases $R_{\min}(M)$, with $\Delta\varepsilon = 0$ corresponding to $R_{\max}$ trajectories (see **Figure 3a**). Further progress in reducing neutron matter EOS uncertainties, and extending results to higher densities, if possible, would further restrict the permitted *M-R* space.

The effects of varying n_m and of reducing the stiffness of the EOS above ε_m are considered in Reference 50. The latter change in the EOS is implemented by reducing the sound speed c_s above the density $\varepsilon_m + \Delta\varepsilon$: $P = (c_s/c)^2(\varepsilon - \varepsilon_m - \Delta\varepsilon) + P_m$. This results in increases in $R_{\min}$ and decreases in $R_{\max}$. **Figure 3b** summarizes the changes for $M_{\max}$, which decreases uniformly with increasing n_m or decreasing sound speed c_s. Neutron star masses above $2.6M_\odot$ are seen to require $c_s^2 > 0.35c^2$ (i.e., the EOS must violate the conformal limit) if $n_m = n_s$, but $c_s^2 > 0.7c^2$ is required if $n_m = 2n_s$. Imposing $M_{\max} > 2.1M_\odot$ and tidal constraints from GW170817 requires $n_m > 1.5n_s$ and $c_s^2 > 0.35c^2$. Alternatively, if $M_{\max} > 2.5M_\odot$, both $n_m > 1.7n_s$ and $c_s^2 > 0.6c^2$ are needed.

Figure 4 shows limiting radii for $1.4M_\odot$ and $2.0M_\odot$ stars as functions of $M_{\max}$ and n_m, assuming $c_s = c$. Smaller values of c_s reduce $R_{\max}$. Note the importance of n_m: If $n_m \gtrsim 2n_s$ and $M_{\max} > 2M_\odot$, then $R_{1.4} < 12.8$ km. Larger radii would mean the EOS is significantly different from the χEFT EOS for densities between n_s and $2n_s$. The difference $R_{2.0} - R_{1.4}$ is especially interesting considering the upcoming agenda of NICER to measure the radii of massive pulsars. Although generally negative, a positive difference requires $n_m \lesssim 2.5n_s$ and $c_s^2 > 0.45c^2$, which could be a signature of a phase transition. As discussed in Section 5, NICER measurements of PSR J0740+6620, coupled with those of PSR J0030+0451, imply $R_{2.0} - R_{1.4} \sim 0.2 \pm 2.0$ km, which is inconclusive.

3. PARAMETERIZATIONS OF HIGH-DENSITY MATTER

Parameterized ε-P functionals are useful tools for probing the uncertain high-density EOS. They have led to useful insights from observations regarding both structural parameters and the underlying EOS. Generally, these parameterizations are subject to constraints: matching to the crust

EOS around $0.5n_s$, causality, thermodynamic stability, satisfaction of the minimum M_{max} from pulsar measurements, and upper and lower bounds suggested by neutron matter calculations in the region of approximately $0.5–2n_s$. A four-parameter phenomenological model (78) is able to accurately reproduce a variety of theoretical dense matter EOSs with an average root mean square residual of order 1%. Coupled to a representative crust EOS, the $M(R)$ relations and M_{max} values could also be reproduced with an average accuracy of better than 2%. These encouraging results have suggested that a viable and efficient inversion technique is the generation of M-R curves that effectively saturate the ε-P or M-R ranges allowed by causality and an assumed M_{max}; from this library, one selects the parameter sets that minimize the differences from the M-R predictions (including uncertainties) from observational data. The optimization is often performed with standard Bayesian techniques. Subsequently, $P(\varepsilon)$ and its uncertainty can be computed.

3.1. Parameterization Models and Constraints

Parameterization schemes normally describe the total pressure–energy density relation for either PNM or β-equilibrium neutron star matter and therefore contain no compositional information. The most frequently used scheme involves piecewise polytropes, in which densities above about $n_0 = 0.5n_s$ are divided into three or more intervals $n_{i-1} < n < n_i$ for $i \in 1 - N$, with the assumed EOS $P = K_i n^{\gamma_i}$ within each interval. Continuity of P and ε at the interval boundaries n_i and ε_i determines K_i. Within each interval, the energy density is

$$\varepsilon = \varepsilon_{i-1}\frac{n}{n_{i-1}} + \frac{Pn_{i-1} - P_{i-1}n}{n_{i-1}(\gamma_i - 1)}. \qquad 11.$$

In this model, the boundary densities n_i as well as the adiabatic indices γ_i are parameters, but the approach used most often is a three-interval, four-parameter (including n_0) one with fixed boundaries $n_1 = 1.85n_s$, $n_2 = 2n_1$, and $n_3 = 4n_1$ (78).

A second frequently used approach consists of Taylor expansions of E_{PNM} around n_s, either in powers of $u = n_B/n_s$ or $u^{1/3}$:

$$E_{PNM}(n) = \sum_{i=0}^{N} a_i u^i \quad \text{or} \quad E_{PNM}(n) = \sum_{i=2}^{N} a_i u^{i/3}. \qquad 12.$$

In the former approach, the N parameters a_i determine

$$S_v = B + \sum_{i=0}^{N} a_i, \quad \frac{L}{3} = \sum_{i=1}^{N} ia_i, \quad \frac{K_N}{9} = \sum_{i=2}^{N} \frac{i!a_i}{(i-2)!}, \quad \frac{Q_N}{27} = \sum_{i=3}^{N} \frac{i!a_i}{(i-3)!}, \quad \text{etc.} \qquad 13.$$

In the latter scheme, which resembles a nonrelativistic Skyrme energy density functional, the kinetic energy fixes $a_2 = 3\hbar(3\pi^2 n_s)^{2/3}/(10m)$, and the other $N - 2$ parameters determine

$$L = \sum_{i=2}^{N} ia_i, \quad K_N = \sum_{i=2}^{N} i(i-3)a_i, \quad Q_N = \sum_{i=2}^{N} i(i-3)(i-6)a_i, \quad \text{etc.} \qquad 14.$$

A third commonly used approach is the spectral decomposition method (79), which is an expansion of the adiabatic index, usually to order $N = 3$:

$$\Gamma(x) = \frac{d\ln P}{d\ln n} = \exp\sum_{i=0}^{N} \gamma_i x^i, \qquad P > P_0, \qquad 15.$$

where $x = \ln(P/P_0)$ and P_0 is the pressure at the core–crust interface. The baryon density n_B is determined from the pressure by

$$n_B(x) = n_0 \exp\int_0^x \frac{dx'}{\Gamma(x')}, \qquad 16.$$

where n_0 is the core–crust interface density. From $d\varepsilon = (\varepsilon + P) \, d \ln n_B$, one obtains

$$\varepsilon(x) = n_B \left[\frac{\varepsilon_0}{n_0} + P_0 \int_0^x \frac{e^{x'} dx'}{n_B(x')\Gamma(x')} \right].$$ 17.

Other approaches are based on constant sound speed or chemical potential segments (80, 81) or on specific physical models, such as relativistic field models (82) with σ, ω, and ρ mesons or quarkyonic models (83, 83a). In contrast to other approaches, constant sound speed segments and quarkyonic models allow for local spikes in sound speed that are motivated by the combination of large M_{max} and relatively small $R_{1.4}$.

3.2. Sensitivity Ranges

Parameterized EOSs can probe the sensitivity of R and M_{max} to the EOS in different density regimes. Reference 84 showed that the pressure of matter in the vicinity of n_s to $2n_s$ is highly correlated with $R_{1.4}$. But the degree of correlation at other densities was not investigated, and the study was limited to a small number of EOSs. Parameterized EOSs can quantify this correlation and extend it to other density ranges and quantities of interest.

One method is to compute the covariance of $A = P(n_B)$ and $B = R_{1.4}, R_{2.0}$, or M_{max}, with means $\bar{A}$ and $\bar{B}$ and standard deviations σ_A and σ_B:

$$C_{A,B} = \sum_{i,j} \frac{(A_i - \bar{A})(B_j - \bar{B})}{\sigma_A \sigma_B}.$$ 18.

The subscript j ranges over all realizations of B for a given EOS parameterization, and i ranges over all values of $P(n_B)$ for which $n_B < n_c$, the central density of the relevant configuration. **Figure 5** shows these correlations for six typical EOS parameterizations (T. Zhao and J.M. Lattimer, manuscript in preparation). **Figure 5** also quantifies the extent to which n_c and the width of its distribution increase with the stellar mass. Notably, the n_c distribution peaks around 30% higher density than for the correlations that involve radii or M_{max}, and the widths of the n_c distributions rapidly increase with the stellar mass. Within any given parameterization scheme,
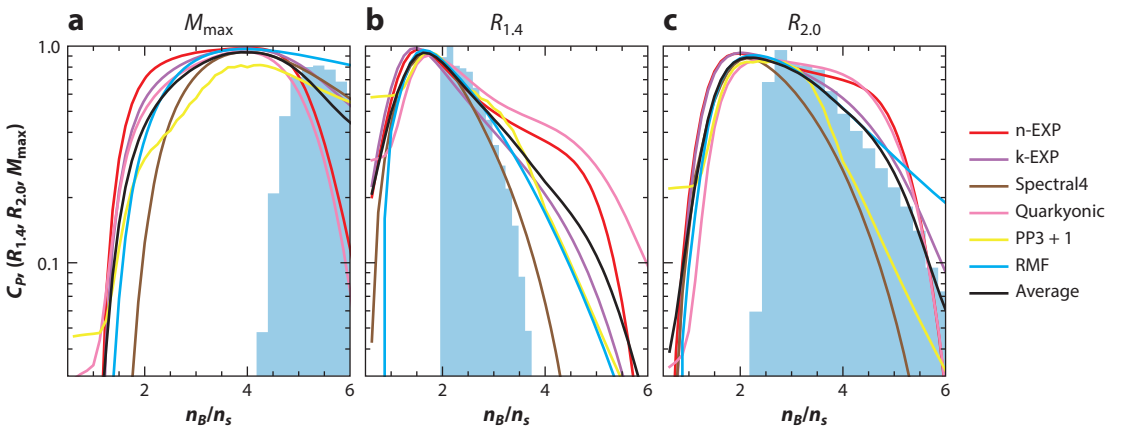
Figure 5

The covariance between the pressure of six different parameterized equations of state at baryon density n_B with (*a*) the neutron star maximum mass and the radii of (*b*) $1.4M_\odot$ and (*c*) $2.0M_\odot$ stars. In each panel, the distribution of central densities for the specified configurations of all the parameterizations is indicated by the blue shading. Figure adapted from Reference 50.

the EOS at a high density is naturally correlated with the EOS at lower densities, so the relatively slow decrease of the covariance at high densities is an artifact of the method.

The correlation between the EOS and $R_{1.4}$ is strongest between n_s and $3.0n_s$, confirming expectations, and the correlation between the EOS and $R_{2.0}$ is strongest at about 40% higher densities. Significantly, these results are relatively insensitive to the parameterization scheme. The standard deviations of both $C_{P,R_{1.4}}$ and $C_{P,R_{2.0}}$ for the six parameterizations are small: $\sigma_R < 0.2$ for all densities and $\sigma_R < 0.05$ near the covariance peaks. This fact demonstrates that knowledge of the EOS near n_s–$2n_s$ (i.e., from χEFT) greatly constrains $R_{1.4}$ and, to a slightly lesser degree, $R_{2.0}$. The situation is different for $M_{\max}$, where the EOS between $2n_s$ and $6n_s$ plays a dominant role and is more uncertain: $\sigma_{M_{\max}} < 0.25$ at all densities and $\sigma_{M_{\max}} < 0.1$ near the covariance peak. Thus, the $M_{\max}$ results are more model-dependent and depend on densities likely above the validity range for χEFT.

3.3. Semiuniversal Relations

Besides the mass and radius, other measurable global properties of neutron stars include binding energies, moments of inertia, tidal deformabilities, and fundamental oscillation mode frequencies. The binding energy $\mathrm{BE} = \mathcal{N} m_B - M$ is the difference between the rest mass $\mathcal{N}$ and the gravitational mass M, where

$$\mathcal{N} = 4\pi \int_0^R n_B r^2 \left(1 - \frac{2GM}{rc^2}\right)^{-1/2} \mathrm{d}r, \quad M = 4\pi \int_0^R \frac{\varepsilon}{c^2} r^2 \mathrm{d}r, \qquad 19.$$

and represents the fractional gravitational mass lost during gravitational collapse of a star from a large radius to R. The equivalent amount of energy could be measured from the neutrinos emitted from a gravitational-collapse supernova, which account for 99% of the newly formed neutron star's binding energy. Estimates obtained from the neutrinos detected from SN 1987A suggested a release of about $(3 \pm 1.5) \times 10^{53}$ erg (85). The moment of inertia could be observed in rare cases in which spin–orbit coupling in a BNS system is detected (86, 87); it is hoped that I eventually will be measured to within 10% uncertainty for the pulsar PSR J0737-3039A. The tidal deformability λ, which is the ratio between the induced dipole moment of a star and an external tidal field, can be extracted from GW signals observed from BNS or BHNS mergers (88, 89). It is usually expressed in terms of the Love number k_2 as $\lambda = 2k_2 R^5/(3G)$. The fundamental oscillation (f-mode) frequency ω_0 is measurable from postmerger high-frequency gravitational radiation and is expected to scale with the mean density as $\sqrt{\bar{\rho}}$ (90). It is convenient to use these quantities in the dimensionless forms BE/M, $\bar{I} = c^4 I/(G^2 M^3)$, $\Lambda = 2k_2 \beta^{-5}/3$, and $\bar{\Omega}_0 = GM\omega_0/c$, where $\beta = GM/(Rc^2)$ is the stellar compactness.

In the Newtonian limit, BE/M, $\bar{I}$, Λ, and $\bar{\Omega}_0$ exhibit universal scalings irrespective of the assumed EOS. For a uniformly dense sphere in the Newtonian limit, one has

$$\mathrm{BE}/M = 3\beta/5, \quad \bar{I} = 2\beta^{-2}/5, \quad \Lambda = \beta^{-5}/2, \quad \bar{\Omega}_0 = \sqrt{4/5}\beta^{3/2}. \qquad 20.$$

It is somewhat more realistic for a neutron star to have the density profile $\rho(r) = \rho_c[1 - (r/R)^2]$, where ρ_c is the central density. This is nearly equivalent, in the Newtonian limit, to an $n = 2$ polytrope; one finds the following:

$$\mathrm{BE}/M = 5\beta/7, \quad \bar{I} = 2\beta^{-2}/7, \quad \Lambda = 2\beta^{-5}/9, \quad \bar{\Omega}_0 \simeq 2.46\beta^{3/2}. \qquad 21.$$

The fact that the expressions for the two cases have the same functional dependence on β but with moderately different coefficients suggests that these quantities obey semiuniversal relations that are relatively insensitive to the underlying EOS. Correlations among structural quantities persist
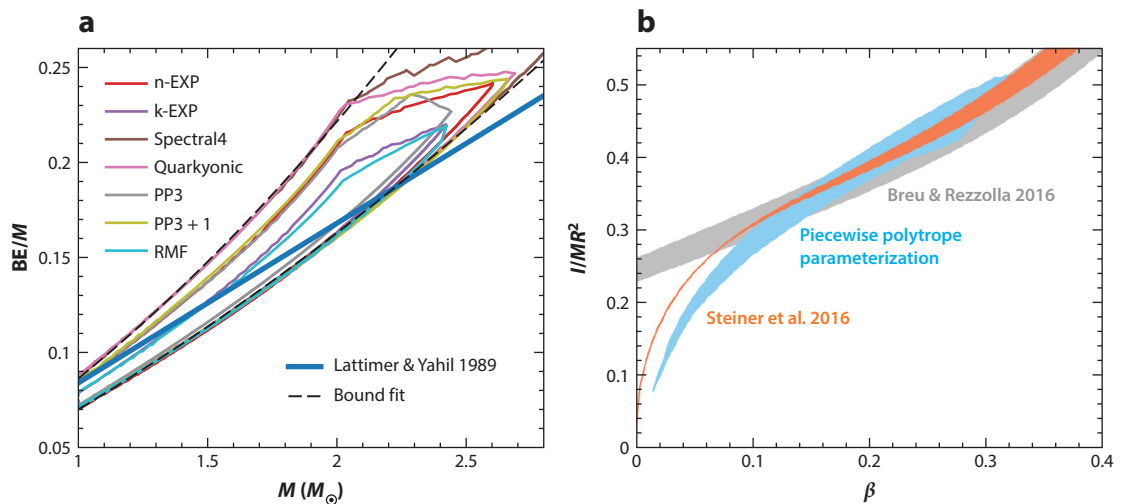
Figure 6

(*a*) The correlation between BE and M for stars with $M \geq 1M_\odot$. Upper and lower bounds are shown for each of several parameterizations constrained by causality, stability, and $M_{max} \geq 2.0M_\odot$. The dark blue curve is a fit from Reference 91. (*b*) The correlation between I/MR^2 and compactness β using a piecewise polytrope parameterization. For comparison, results are shown from Steiner et al. (93) and Breu & Rezzolla (94). Panel adapted from Reference 92; copyright 2020 The American Astronomical Society.

in general relativity and can be tightened if additional constraints, such as causality and a minimum M_{max}, are imposed. Parameterized EOSs provide convenient tools to quantify and, more importantly, bound these relations. Therefore, observations regarding one or more structural properties can inform other structural observables and the underlying EOS with quantifiable uncertainties. Because these structural properties are strongly dependent upon R, their covariances resemble those of C_{P,R_M} (**Figure 5**).

Figure 6a shows a semiuniversal relation involving BE obtained from parameterized EOSs subject to constraints including stability, causality, the validity of χEFT PNM up to $2n_s$, and $M_{max} \geq 2.0M_\odot$. Results are bounded by the following (T. Zhao and J.M. Lattimer, manuscript in preparation):

$$\text{BE}/M \simeq a_B M + b_B M^2 = (0.0602 \pm 0.0016)M + (0.0180 \pm 0.0065)M^2, \qquad 22.$$

where M on the right-hand sides is in solar units. **Figure 6b** compares a semiuniversal relation involving I obtained from parameterized piecewise polytrope EOSs (92) with those of References 93 and 94. Note that $M > 1M_\odot$ requires $\beta \gtrsim 0.1$, so the divergences at lower β values are inconsequential. It is worth replotting the $\bar{I}$-β correlation as shown in **Figure 7a** so that it becomes evident that $\bar{I}\beta^{3/2} \simeq 0.087 \pm 0.005$ is bounded to within about $\pm6\%$, revealing that neutron stars approximately obey $I \propto (MR)^{3/2}$. It is, however, even more remarkable that $\bar{I}$ and Λ have an extremely tight correlation, known as the I-Love relation (95), which is accurate to better than 0.5% in the region of interest (**Figure 7b**). A similarly tight correlation between $\bar{I}$ and the quadrupole moment has already proved useful in reducing the parameter space in pulse-profile modeling (Section 5).

The definition of the tidal deformability suggests $\Lambda \propto \beta^{-5}$. However, the Love number k_2 is roughly proportional to β^{-1} (96) for $\beta \gtrsim 0.1$ ($M \gtrsim 1M_\odot$); for smaller β, k_2 increases rapidly with β. Therefore, it is not surprising that $\Lambda\beta^6 \simeq 0.009 \pm 0.002$ is constant to within 20% (**Figure 8a**).
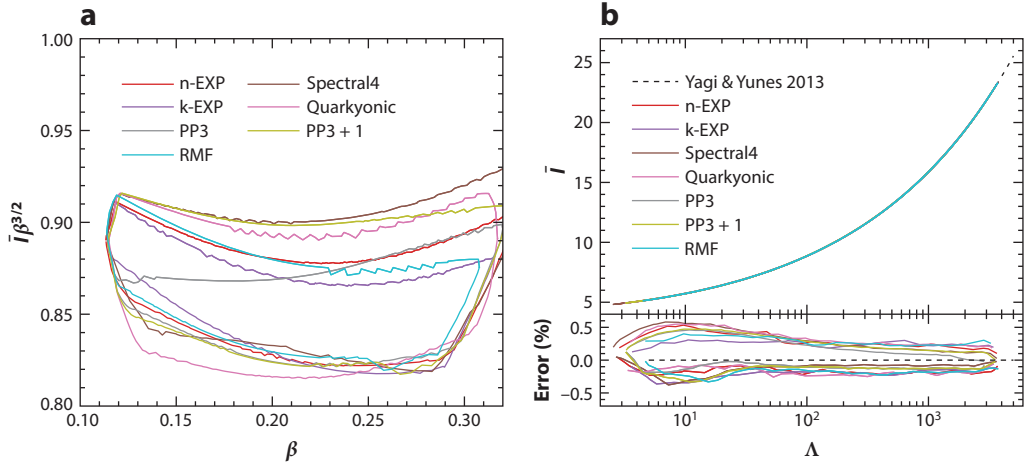
Figure 7

(*a*) The correlation between $\bar{I}$ and β for stars with $M \geq 1 M_\odot$. Upper and lower bounds are shown for each of several parameterizations. (*b*) The nearly universal Λ-$\bar{I}$, or I-Love, correlation, with the largest deviations between the relation given in Reference 95 (Yagi & Yunes 2013) and various parameterized equations of state as a function of Λ illustrated in the subpanel.
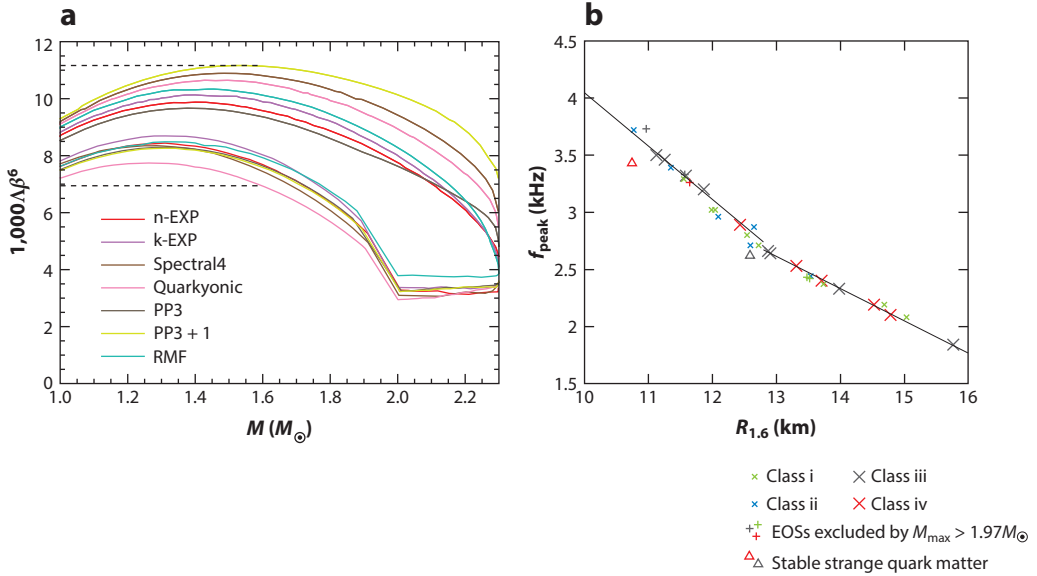
Figure 8

(*a*) The quantity $\Lambda\beta^6$ as a function of mass M. The dashed horizontal lines indicate that for the range of masses inferred for the components of GW170817 ($1.0 M_\odot < M < 1.6 M_\odot$), this quantity is approximately constant with value $\Lambda\beta^6 = 0.009 \pm 0.002$. (*b*) The EOS-insensitive correlation of the fundamental oscillation frequency of a postmerger remnant with $R_{1.6}$, the radius of a $1.6 M_\odot$ star, assuming no strong phase transitions. Class i consists of EOSs with consistent temperature treatments. Class ii consists of barotropic microphysical EOSs (without temperature and electron fraction dependence). Class iii is the same as class ii but fitted with piecewise polytropes. Class iv consists of microphysical low-density EOSs with high-density piecewise polytropic extensions. Classes ii–iv have thermal effects mimicked by an ideal-gas component. Plus signs indicate EOSs that are excluded by $M_{max} > 1.97 M_\odot$. Triangles indicate stable strange quark matter EOSs. Panel adapted with permission from Reference 97. Abbreviation: EOS, equation of state.

The lower limit of the bound increases with M_{max}; for $M_{max} \gtrsim 2.3 M_\odot$, $\Lambda \beta^6 \simeq 0.0095 \pm 0.0015$. This semiuniversal behavior can be used to render EOS-insensitive interpretations of GW signals.

There are semiuniversal correlations between the fundamental oscillation frequency $\bar{\Omega}_0$ and M and R (90, 97, 98). An even tighter correlation existing between $\bar{\Omega}_0$ and $\bar{I}$ (99) could supplement inferences from the tidal deformability. The dominant frequency f_{peak} observed in simulations of the post-BNS merger GW spectrum (97) is probably equivalent to $2\pi\omega_0$, and it shows a strong correlation with $R_{1.6}$ (**Figure 8b**).

4. OBSERVATIONS OF COMPACT STAR MERGERS

One of the most exciting recent developments is the GW detection of BNS and possibly BHNS mergers. GW170817 (28), the first BNS merger detected, is especially important because of its multimessenger nature: It was accompanied by a short γ-ray burst (100, 101) and a kilonova (see, e.g., 102). The short time delay between the merger and the γ-ray burst, about 1.7 s, implied the collapse of the merger remnant into a black hole on a smaller timescale. The kilonova was caused by the radioactive decay of expanding material ejected during and after the merger; it was first detected 14 h after the merger, but this delay was due to logistics. This EM radiation had the signature (103, 104) long anticipated to accompany the r-process nucleosynthesis that is thought to occur in both BHNS and BNS mergers (105). Kilonovae have not yet been observed to accompany other mergers, likely because of their much greater distances. For an extensive review of the dynamics of neutron star mergers, readers are referred to Reference 12.

The GW signal from a merger contains information concerning the masses of the components as well as their sizes. In general relativity, radiation reaction generates GWs that radiate orbital energy, resulting in inspiral of the components. During inspiral, the GWs are expected to have a sinusoidal behavior: Both the frequency f (equal to twice the orbital frequency) and amplitude h increase with time up to the merger, producing a so-called chirp signal (**Figure 9**). The evolution of h, f, and f's time derivative $\dot{f}$ constrains the system's chirp mass $\mathcal{M}$ and distance D:

$$\mathcal{M} = \frac{(m_1 m_2)^{3/5}}{(m_1 + m_2)^{1/5}} = \frac{c^3}{G} \left(\frac{5\dot{f}}{96f} \right)^{3/5} \left(\frac{1}{\pi f} \right)^{8/5}, \quad D = \frac{5c}{48\pi^2} \frac{\dot{f}}{h f^3}. \qquad 23.$$

The expression for D ignores a degeneracy with the orbit's inclination relative to the observer, but detection with multiple instruments and/or an EM determination of a precise sky location can partially break this degeneracy. The mass ratio $q = m_2/m_1$ cannot be determined nearly as

Binary neutron star signal

| Contact | Merger | Postmerger | Collapse to black hole |
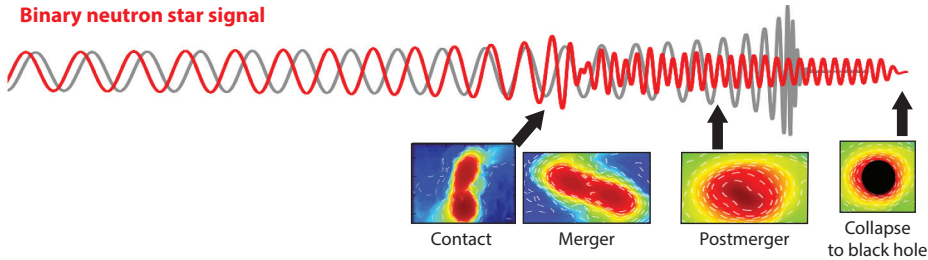
Figure 9

Illustration of the gravitational wave signal expected from a binary neutron star merger (*red curve*) compared with a binary black hole merger (*gray curve*) with the same chirp mass $\mathcal{M}$. Tidal deformation accelerates infall and causes an advance in the binary neutron star gravitational wave phase. The epochs corresponding to contact, merger, postmerger, and collapse to a black hole are indicated by arrows and images along the bottom. Figure provided by T. Dietrich.

accurately as $\mathcal{M}$; its lower limit may be more effectively realized using prior assumptions about the minimum and maximum neutron star masses.

In binary black hole (BBH) mergers, the components are essentially point particles from the gravitational point of view. For a merger that involves neutron stars, finite-size effects have to be considered. Tidal deformations are the largest finite-size effects, and they cause a more rapid orbital decay. The lowest-order instantaneous change to the GW phase is (106)

$$\delta\Phi = -\frac{117}{256}\frac{(1+q)^4}{q^2}\left(\frac{\pi f G\mathcal{M}}{c^3}\right)^{5/3}\tilde{\Lambda},$$

24.

where $\tilde{\Lambda}$ is the binary deformability, a mass average of Λ_1 and Λ_2,

$$\tilde{\Lambda} = \frac{16}{13}\frac{(1+12q)\Lambda_1 + (12+q)q^4\Lambda_2}{(1+q)^5}.$$

25.

Radii in the relevant mass range $1.1M_\odot < M < 1.6M_\odot$ for BNS mergers have relatively small variations from a mean value $\bar{R}$ for a given EOS. Reference 107 found, using piecewise polytropes, that in the absence of a significant phase transition, $|\bar{R} - R| < 0.5$ km with a standard deviation $\sigma_R \simeq 0.1$ km. Since $\Lambda = a\beta^{-6}$, with $a = 0.009 \pm 0.002$ from **Figure 8**, assuming a fixed $R(M) \simeq \bar{R}$ implies $\Lambda_1 \simeq q^6\Lambda_2$. It therefore follows that

$$\tilde{\Lambda}_{\mathcal{M}} \simeq \frac{16a}{13}\left(\frac{\bar{R}c^2}{G\mathcal{M}}\right)^6\frac{q^{8/5}(12 - 11q + 12q^2)}{(1+q)^{26/5}} = (0.0040 \pm 0.0006)\left(\frac{\bar{R}c^2}{G\mathcal{M}}\right)^6,$$

26.

where Λ_M and $\bar{\Lambda}_{\mathcal{M}}$ denote that Λ and $\bar{\Lambda}$ are measured for a particular M or $\mathcal{M}$, respectively. Causal parameterized EOSs with $q > 0.6$ and $M_{max} > 2M_\odot$ provided the bounds in Equation 26 (107). The q dependence in Equation 26 is very weak: $\tilde{\Lambda}_{\mathcal{M}}(q = 0.7)/\tilde{\Lambda}_{\mathcal{M}}(q = 1.0) = 1.029$. It naturally follows that

$$\Lambda_M \simeq 2^{6/5}(\mathcal{M}/M)^6\tilde{\Lambda}_{\mathcal{M}},$$

27.

which is useful, for example, if one wants to estimate the deformability of a $1.4M_\odot$ star from a measurement of $\tilde{\Lambda}_{\mathcal{M}}$. The q dependence of Equation 24 is nearly as weak as for $\tilde{\Lambda}$: $\delta\Phi(q = 0.7)/\delta\Phi(q = 1) = 1.10$. Partially, this weak dependence is due to the fact that both $\partial\tilde{\Lambda}_{\mathcal{M}}/\partial q$ and $\partial\delta\Phi/\partial q$ vanish in the limit $q \to 1$. It further follows that

$$\bar{R} \simeq (11.3 \pm 0.3)\frac{\mathcal{M}}{M_\odot}\left(\frac{\tilde{\Lambda}_{\mathcal{M}}}{800}\right)^{1/6}\text{ km}.$$

28.

Because of radius correlations, the uncertainty is only half that expected from the uncertainty in a. Since $\mathcal{M}$ is likely to be well measured, $\tilde{\Lambda}_{\mathcal{M}}$ carries significant radius information.

4.1. GW170817

The observation of GW170817 opened a new window onto neutron stars. The final stages of the inspiral illustrated in **Figure 9** could not be observed because of a loss of detector sensitivity at frequencies beyond about 500 Hz. But GW170817's chirp mass $\mathcal{M} = (1.186 \pm 0.001)M_\odot$ was accurately measured because the duration τ of the event and the number $\mathcal{N}$ of observed orbits were large:

$$\tau = \frac{5}{256}\left(\frac{c^3}{G\mathcal{M}}\right)^{5/3}\left(\frac{1}{\pi f_d}\right)^{8/3} \simeq 317\text{ s}, \quad \mathcal{N} = \frac{16}{5}f_d\tau \simeq 1.01 \times 10^4,$$

29.

where $f_d = 20$ Hz was the initial (lowest) observed frequency with a usable signal. For equal-mass components, tidal disruption occurs before contact when the separation r reaches the Roche limit

$r_R \simeq 2.63R$ in Newtonian gravity. General relativity alters this estimate minutely: $r_R \simeq 2.72R$ (108). Therefore, tidal disruption happens at the frequency f_R:

$$f_R \simeq \frac{c}{\pi} \left(\frac{GM2^{6/5}}{r_R^3 c^2} \right)^{1/2} = 1.03 \text{ kHz}. \qquad 30.$$

Postmerger oscillations have GW frequencies of order 3 kHz (**Figure 8b**), so it is doubly imperative that future detectors have an improved high-frequency response; the Neutron Star Extreme Matter Observatory (NEMO) (109) is one such design. The initially measured GW170817 distance had an uncertainty of order 25%, but using the EM information concerning sky location reduced that by more than a factor of two.

The fortuitous discovery of an associated short γ-ray burst and kilonova in the galaxy NGC 4993 added enormously to GW170817's significance. Both were observed within the GW sky location uncertainty window, and NGC 4993 matches the GW distance. The appearance of a kilonova not only seems to confirm that most of the r-process elements (which account for about half of all heavy nuclei) are synthesized in mergers that involve neutron stars but also provides theoretical support for an upper limit to $M_{\max} \sim 2.2\text{–}2.3M_\odot$ (Section 4.2).

The LIGO/Virgo Collaboration (LVC) initially reported an upper 90% confidence limit[3] $\tilde{\Lambda}_{1.186} \simeq 800$ (28). Because $\tilde{\Lambda}$ has a nearly 100% relative uncertainty, most studies of EOS constraints have focused not on its mean value but on its 90% upper confidence bound. Using the lower bound for a and $q \sim 1$ in Equation 26, it follows that $\bar{R} \lesssim 13.4$ km, similar to the estimate of 13.5 km found in Reference 28.

There are 13 fitting parameters in the sixth-order post-Newtonian TaylorF2 (110, 111) waveform model that LVC used; finite-size effects first appear at fifth order. Extrinsic parameters include two for the sky location and one each for distance, inclination, the coalescence time and phase, and the signal's polarization; intrinsic parameters include two each for the component masses, spins, and tidal deformabilities. Reference 112, alternatively, fixed the sky location and distance from EM observations and also implemented the correlation $\Lambda_2 = q^6 \Lambda_1$ justified in Section 3.3. Ignoring the existence of a Λ-m correlation is tantamount to assuming that the neutron stars possibly obey different EOSs, which should not be the case unless a strong phase transition exists in the interval between their central densities. This interval is small since the most likely value of q is approximately 0.9–0.95. The consequent overall reduction to nine fitting parameters reduced the upper confidence limit to $\tilde{\Lambda}$ and identified a nonzero lower bound (**Figure 10**). Subsequent analyses (113, 114) incorporating EOS correlations confirmed these results. Reference 113 also demonstrated that the choice of waveform model leads to insignificant systematic uncertainty.

Figure 10 shows the GW170817 probability distribution function (PDF) for $\tilde{\Lambda}$ and q from Reference 112 with their marginalized one-dimensional distributions. The mean value of $\tilde{\Lambda}$ is about 235, and its upper 90% confidence bound is about 645—near the bound of 720 given by Reference 113. The Bayesian analysis assumed uniform priors for m_2 and $m_1 > m_2$ in the range $M_\odot$–$2M_\odot$ and a uniform prior for $\sqrt{\Lambda_1 \Lambda_2}$ in the range 1–3,000. This analysis did not take into account any nuclear physics priors. However, if one uses parameterized EOSs (107), the UGC imposes a lower limit $\tilde{\Lambda}_{1.186} > 200$ if $M_{\max} \sim 2M_\odot$, which appears to remove nearly 40% of the probability weight at lower $\tilde{\Lambda}$ values. The inferred $\tilde{\Lambda}$ upper limits would increase if this conjecture were implemented as a prior.

---

[3]Reference 28 defined this limit to mean that 10% of the probability lies above the upper limit, but when there is a lower limit, it actually corresponds to a contour enclosing 80% of the total weight. Subsequently, this convention is not used in this review.
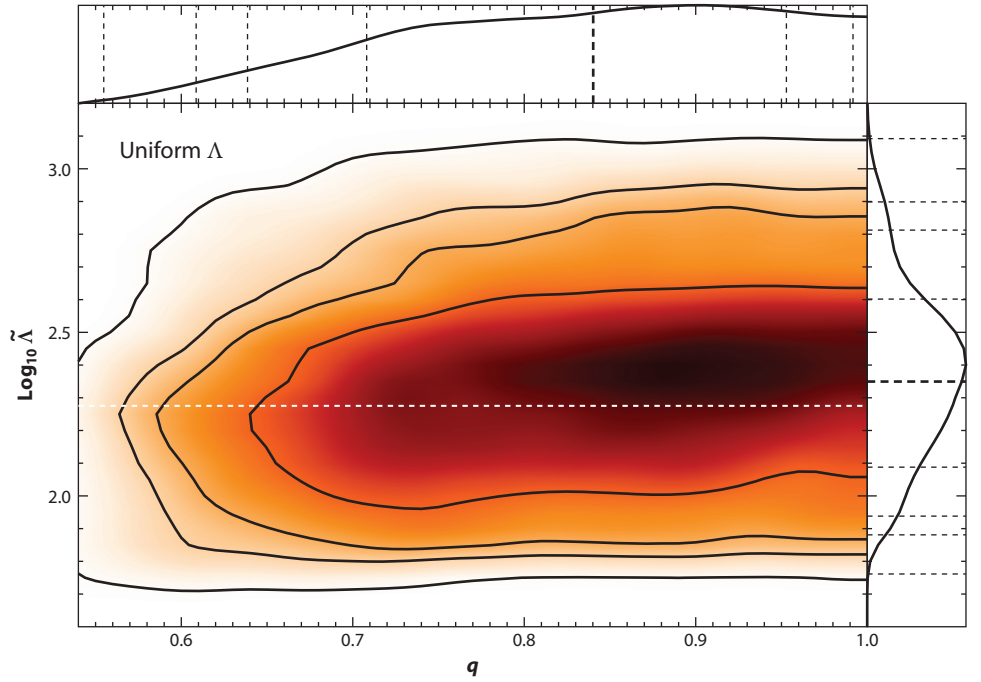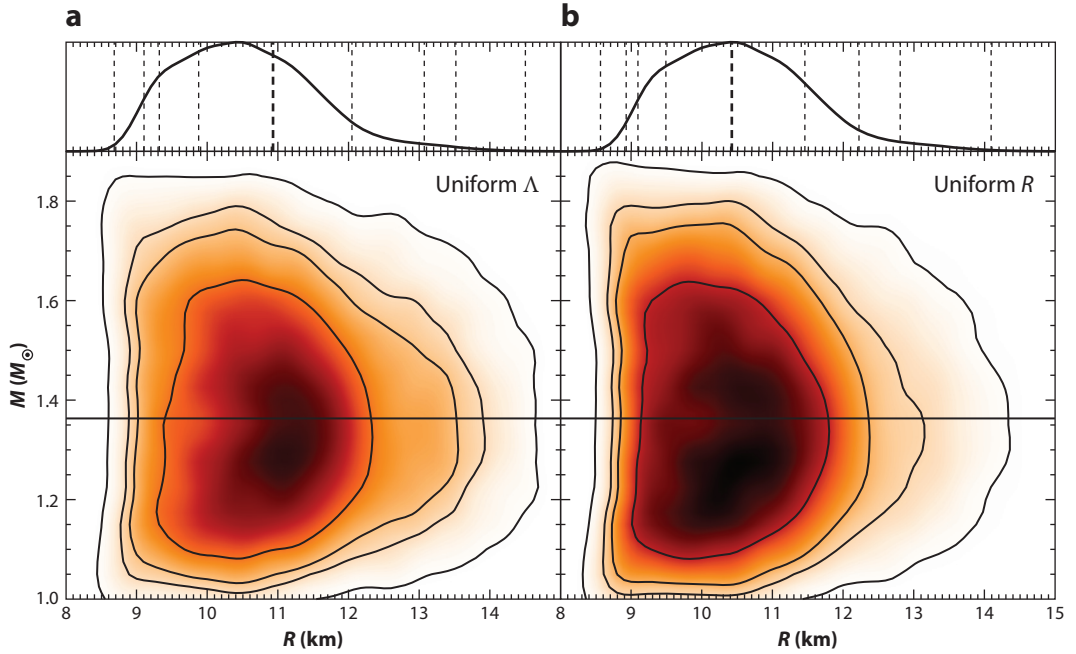
Figure 10

Probability distribution function for $\tilde{\Lambda}_{1.186}$ and q for GW170817, assuming a uniform prior in $\sqrt{\Lambda_1 \Lambda_2}$. Contour lines enclose 68.27%, 90%, 95.45%, and 99.73% of the total weight. The white dashed line indicates the minimum $\tilde{\Lambda}$ consistent with the Unitary Gas Conjecture. The subplot at the top shows the marginalized probability distribution function for q, and the subplot on the right shows the marginalized probability distribution function for $\tilde{\Lambda}$. In each subplot, the bold dashed lines indicate the mean and the light dashed lines enclose the same percentage weights as in the main figure. Data from Reference 112.

Using these PDFs together with the relation shown in Equation 28 allows distributions in *M-R* space to be drawn. **Figure 11a** shows results found when assuming a uniform prior in masses and deformabilities, as was assumed in Reference 28 and **Figure 10**. The 90% confidence bound is 9.3 km $< \bar{R} <$ 13.1 km with a mean of 10.9 km. Alternatively, one could assume a uniform radius prior, which, because of the approximate relation $\Lambda \propto R^6$, is effectively a uniform distribution in $\ln(\Lambda_1 \Lambda_2)$ and might be preferred because of the large dynamic range of $\Lambda_1 \Lambda_2$. This prior increases weights of smaller values of $\tilde{\Lambda}_{\mathcal{M}}$, and therefore R, which, as displayed in **Figure 11b**, implies the 90% confidence bound 9.1 km $< \bar{R} <$ 12.2 km with a mean of 10.4 km. This ambiguity in the prior represents a systematic uncertainty of nearly a full kilometer in the upper confidence bound—consistent with the analysis of Reference 114, which used a $\tilde{\Lambda}$ prior based on a set of EOSs giving a uniform distribution in $R_{1.4}$. The moderate signal-to-noise ratio for GW170817 makes assumptions concerning the EOS or the prior Λ distributions to remain moderately important.

It is anticipated that the moment of inertia of the more massive member of the double pulsar PSR J0737-3039 will soon be measured (87). Since the 1.338$M_\odot$ mass of PSR J0737-3039A and the component masses of GW170817 are nearly the same, the GW170817 Λ-M PDFs can be combined with the universal *I*-Love relation (95) shown in **Figure 7** to predict $\Lambda_{1.338} = 267^{+624}_{-195}$ and $\bar{I}_{1.338} = 57.9^{+19.8}_{-15.2}$ if a uniform prior in $\sqrt{\Lambda_1 \Lambda_2}$ is assumed and $\Lambda_{1.338} = 234^{+236}_{-156}$ and $\bar{I}_{1.338} = 56.1^{+10.9}_{-12.8}$ if a uniform prior in $\ln(\Lambda_1 \Lambda_2)$ is assumed. Comparison with the actual measurement of $\bar{I}$ for PSR J0737-3039A will provide an important consistency check for these independent

Figure 11

Probability distribution functions for M and R for GW170817, assuming uniform priors in $\sqrt{\Lambda_1\Lambda_2}$ (*a*) and R (*b*). Contour lines enclose 68.27%, 90%, 95.45%, and 99.73% of the total weight. The subplots at the top show the marginalized R probability distribution function; in each subplot, the bold dashed lines show the mean and the light dashed lines enclose the same weights as in the main figure. Data from Reference 112.

observations. A significant discrepancy could indicate the existence of a phase transition above the central density of a $1.36 M_\odot$ star.

4.2. Multimessenger Inferences for the Maximum Mass

Bright kilonovae require the formation of a significant postmerger disk. Whether this or an alternate immediate collapse into a black hole occurs depends on M_{max}, the binary mass ratio q, and the neutron star compactness β. From the results of multiple numerical simulations that varied these parameters, Reference 115 concluded that immediate collapse ensues if

$$M_T \gtrsim M_{max} \left(2.38 - 3.606 \frac{G M_{max}}{R_{1.6} c^2} \right). \qquad 31.$$

The minimum radius $R_{1.6}$ of a $1.6 M_\odot$ star needed for disk formation turns out to be insensitive to assumptions concerning both q and M_{max} for a given value of $\mathcal{M}$. For GW170817, assuming an $M_{max} > 2 M_\odot$ gives $R_{1.6} > 10.3$ (10.7) km if $q = 1$ (0.7), which is almost the same as the 10.35-km minimum radius implied by the UGC lower limit of $\tilde{\Lambda}_{1.186} \simeq 200$ (**Figure 10**). This minimum radius virtually guaranteed the formation of a disk and kilonova for GW170817. By contrast, Reference 116 estimated a lower limit $\tilde{\Lambda}_{1.186} \gtrsim 400$ in order to satisfy both EM and GW constraints for GW170817. Reference 117 argued that the lower limit should be smaller: $\tilde{\Lambda} \gtrsim 250$, corresponding to $\bar{R} \geq 10.7$ km, which agrees with the above limits.

Model simulations have long suggested that BNS mergers should lead to dynamical mass ejection irrespective of whether a black hole is ultimately formed. Additional mass ejection seems to

occur from the coalesced, rapidly rotating massive neutron star and its centrifugally supported disk. Immediate collapse to a black hole on a millisecond timescale following the merger might preclude the large amount of ejected mass, $\gtrsim 0.05 M_\odot$, inferred by the luminosity and duration of the kilonova connected with GW170817. However, a short delay before collapse of no more than a second is suggested by the appearance of a short γ-ray burst, which is thought to require the environment of disk accretion onto a black hole.

According to simulations, the initial angular momentum of the coalesced remnant of a binary with initial gravitational mass $M_T = \mathcal{M} q^{-3/5}(1+q)^{6/5}$, chiefly coming from the orbital angular momentum, is $J = (4.041 M_T - 4.658 M_\odot) G M_\odot / c$ (115). Therefore, its Kerr parameter $a/M_T = c J/(G M_T^2) \simeq 0.86$ for $M_T = 2.73 M_\odot$. However, the mass-shedding (Keplerian) limiting spin frequency is $f_K \simeq 0.094 \sqrt{GM/R^3}$ Hz for a uniformly rotating star, which limits $a/M \leq 0.70$ (118). Thus, the remnant is initially differentially rotating, with massive winds driving mass and angular momentum into a disk (119). If M_T is not too large, the remnant will have sufficient centrifugal and magnetic support to forestall collapse at least until it regularizes into uniform rotation, which might take a few hundred milliseconds. A uniformly rotating star, with $f < f_K$, could survive for minutes to years because its angular momentum loss is relatively slow. Such prolonged survival would have been unlikely for GW170817 because, in addition to preventing the formation of a kilonova and a γ-ray burst, a long-lived stable remnant would generate a huge spin-down luminosity that would dramatically heat the expanding ejecta (29), a feature that is not evident in the kilonova light curve. The maximum mass of a differentially rotating star is $M_d \sim 1.5 M_{max}$, which follows from Equation 31 using $M_{max} = (2.0–2.2) M_\odot$ and $R_{1.6} \simeq 12$ km. For comparison, the maximum mass that can be supported by uniform rotation is $M_u = \xi M_{max}$, where $1.16 < \xi < 1.20$ depends on the EOS (120).

During the merger, baryon mass, not gravitational mass, is conserved because of binding energies. The semiuniversal relation shown in Equation 22 can be used to relate M_T to the total baryon mass (M_{BT}) of the coalesced, differentially rotating remnant:

$$M_{BT} = M_T + a_B(1+q^2)/(1+q)^2 M_T^2 + b_B M_T^3 (1+q^3)/(1+q)^3 - \Delta M, \qquad 32.$$

where $\Delta M \sim 0.05 M_\odot$ is the ejected mass. Simulations indicate that the factor ξ also applies to baryon masses. Therefore, the EM and GW observations can be reconciled if the total baryon mass M_{BT} obeys

$$\xi M_{Bmax} < M_{BT} < M_{Bd}, \qquad 33.$$

where $M_{Bmax} = M_{max} + a_B M_{max}^2 + b_B M_{max}^3$ is the maximum baryon mass of nonrotating neutron stars. In this way, the remnant survives as a short-lived hypermassive star until losing enough angular momentum to trigger collapse; it never becomes a long-lived supermassive star. For $q > 0.7$, $\xi > 1.16$, and $\Delta M > 0$, multimessenger observations of GW170817 therefore suggest $M_{max} \lesssim 2.23 M_\odot$, which is compatible with other estimates (29, 121–124). This estimate implies a gap of perhaps 0.1–0.2 $M_\odot$ between the upper and the existing lower bounds to M_{max}.

4.3. Further Detections and Expectations

There are 17 BNS systems in our Galaxy with measured M_T (21, 125), of which 10 have orbital decay times less than the Hubble time t_H and, if Galactic BNS systems are characteristic of the extra-Galactic distribution, would represent the population relevant for potentially observable mergers. The distribution of these 10 BNS systems has a mean $M_T = 2.69 \pm 0.12 M_\odot$. Kernel density estimation yields a non-Gaussian distribution with a mean $M_T = 2.66^{+0.18}_{-0.11} M_\odot$ (**Figure 12a**). For comparison, GW170817 seems typical; assuming $q = 1$, it has $M_T = 2.73 M_\odot$. The condition
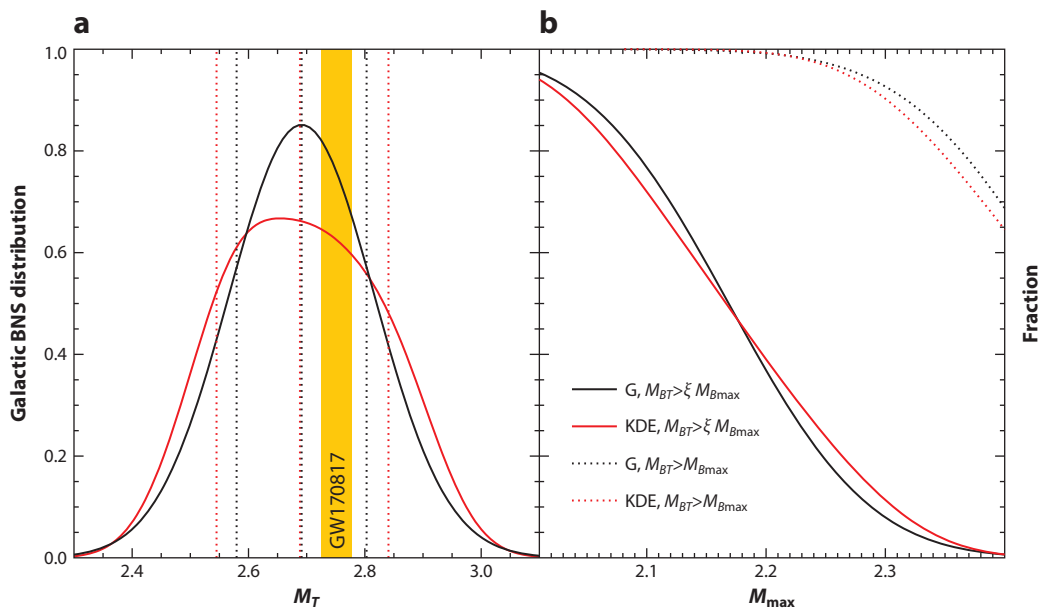
Figure 12

(*a*) Probability distributions for Galactic BNS systems. The gold band indicates the inferred M_T for GW170817. The black curve shows a fitted Gaussian, and the red curve shows the fit from KDE. Vertical dotted lines show the respective mean M_T and ± 1 standard deviations. (*b*) The dotted curves show the fraction of time that a metastable remnant is expected to form in a BNS merger as a function of M_{max}. The solid curves show the chances that the remnant will be hypermassive. The differences between the dashed and solid curves show the chances that the remnant will be supramassive, resulting in extra heating of the ejecta. Abbreviations: BNS, binary neutron star; G, Gaussian; KDE, kernel density estimation.

$M_{BT} < M_{Bd}$ is virtually guaranteed for all BNS mergers, since $M_{max} > 2M_\odot$ implies $M_T > 3.2M_\odot$. This condition is roughly equivalent to Equation 31, as noted previously. Immediate remnant collapse to a black hole should never occur. It is possible to estimate what fraction of BNS mergers might produce stable neutron stars ($M_{BT} < M_{Bmax}$), supramassive neutron stars ($M_{Bmax} < M_{BT} < \xi M_{Bmax}$), or hypermassive neutron stars ($M_{BT} > \xi M_{Bmax}$), such as seemingly applies to GW170817.

Figure 12*b* shows the critical $M_T(M_{max})$ relation established from $M_{BT} = M_{Bmax}$ (dotted lines) and $M_{BT} = \xi M_{Bmax}$ (solid lines) for the observed Galactic BNS distribution having orbital decay times less than t_H. If $M_{max} < 2.2M_\odot$, then nearly all BNS mergers form metastable neutron stars with $M_{BT} > M_{Max}$, and at least 40% form hypermassive remnants that quickly collapse to black holes. The remainder may form supramassive magnetars that contribute greatly to heating of the kilonova ejecta. The kilonova associated with GRB200522A (126) may be an example; it was about 10 times more luminous than GW170817 and too bright to be explained solely by radioactive decay from r-process nuclei.

The observed decay time distribution of the 10 Galactic BNS systems with decay times less than the Hubble time is interesting: 10% would have $\tau_{decay} < 47$ Myr, 20% would have $\tau_{decay} < 77$ Myr, and 50% would have $\tau_{decay} < 250$ Myr. The large fractions of systems with relatively short decay times (if this distribution is universal) and the relatively low upper limit to M_{max} deduced from GW170817 both support the hypothesis that mergers are a substantial source of r-process nucleosynthesis (105).

Further evidence for $M_{max} \lesssim 3M_\odot$ comes from the discovery of a dark companion of mass $3.04 \pm 0.06M_\odot$ to the red giant V723 Mon (127, 128), and a likely black hole of mass $3.3^{+2.8}_{-0.7}M_\odot$

is orbiting the red giant 2MASS J05215658+4359220 (135). However, it should be noted that a similar previous discovery of a low-mass dark companion was suggested to be due to a low-mass stellar binary (129). Perhaps the best evidence for $M_{max} < 3M_\odot$ comes from GW detections.

There were 39 mergers identified in the first half of the O3 LVC run (April–October 2019) that were above the signal-to-noise threshold (false alarm rate >2 per year), including 36 BBH systems (130). The remaining three events, GW190425 ($\mathcal{M} = 1.44 \pm 0.02M_\odot$) (131), GW190426 ($\mathcal{M} = 2.41^{+0.08}_{-0.18}M_\odot$) (130), and GW190814 ($\mathcal{M} = 6.09 \pm 0.06M_\odot$) (132), potentially contain neutron stars. GW190425 has estimated masses that depend on the spin prior assumptions. In the case of a low-spin prior, which is favored for BNS systems, $m_1 = 1.73^{+0.14}_{-0.13}M_\odot$ and $m_2 = 1.57^{+0.12}_{-0.11}M_\odot$, meaning that both stars have larger masses than are seen in the Galactic BNS distribution. In fact, M_T is several standard deviations higher than the mean of the Galactic BNS distribution. With a high spin prior, which is more appropriate for BHNS systems, it is found that $m_1 = 2.06^{+0.46}_{-0.45}M_\odot$ and $m_2 = 1.40^{+0.28}_{-0.28}M_\odot$, which could be compatible with a typical neutron star paired with a black hole slightly above the upper limit to M_{max} deduced from GW170817. For comparison, Reference 133 (see also Reference 134) assumed priors compatible with a BNS system to find $m_1 = 1.85^{+0.27}_{-0.19}M_\odot$ and $m_2 = 1.47^{+0.16}_{-0.08}M_\odot$ and, for priors compatible with a BHNS system, $m_1 = 2.19^{+0.21}_{-0.17}M_\odot$ and $m_2 = 1.26^{+0.10}_{-0.08}M_\odot$. The black hole would have a very small mass, below the traditional mass gap of 3 to $5M_\odot$. However, the binary V723 Mon has recently been shown to contain a black hole of mass $2.95 \pm 0.17M_\odot$ (127, 128). Furthermore, supernova simulations give no reason why a black hole could not form between M_{max} and $5M_\odot$. No EM counterpart was detected in GW190425, but the estimated 160-Mpc distance and the 10,000-square-degree sky uncertainty could have prevented a kilonova detection. And if it was a BNS merger, its total mass $M_T > 3.26M_\odot$ would likely exceed M_d, prompting an immediate postmerger collapse to a black hole. In either case, inferred tidal deformabilities (131) are noninformative, predicting $R_{1.4} < 17.5$ km in the BNS case and $R_{1.4} < 15.7$ km in the BHNS case.

The case of GW190814 is also compelling. Its masses are estimated as $m_1 = 23.2^{+1.1}_{-1.0}M_\odot$ and $m_2 = 2.59^{+0.08}_{-0.09}M_\odot$. While it is possible that this is a BHNS system, m_2 would significantly exceed the upper limit to M_{max} deduced from GW170817. No EM counterpart was detected, but the extreme mass ratio makes the likelihood of mass ejection and a kilonova very small, and its estimated 240-Mpc distance would make afterglow detection difficult. It appears more likely that this is an extreme-mass-ratio ($q \sim 0.11$) BBH merger, again with a low-mass black hole in the mass gap. If this system could be proved to contain a neutron star, the implications would be profound (50, 136–143), as indicated in Section 2.4.

GW190426 (130) is a low-signal-to-noise BHNS candidate announced in GCN Circulars (144); these reports include estimates of its relative probability of being in the LVC classes of BNS (both stars <$3M_\odot$; 25%), gap (at least one star between 3 and $5M_\odot$; 15%), BHNS (one star <$3M_\odot$ and one star >$5M_\odot$; 60%), and BBH (both stars >$5M_\odot$; 0%), and also an estimated 72% probability that disruption led to the formation of a disk that survived for at least a few tenths of a second. The system's chirp mass, although well measured at detection, was not released for 18 months because of LVC policy. Nevertheless, from the available probability information, and assuming that q was very uncertain, Reference 145 accurately predicted $\mathcal{M} \sim 2.4M_\odot$ with the most likely configuration consisting of a 1.3–1.5$M_\odot$ neutron star and an ∼$6M_\odot$ black hole. Eventually, LVC (130) confirmed these estimates, finding $m_1 = 5.7^{+4.0}_{-2.3}M_\odot$ and $m_2 = 1.5^{+0.8}_{-0.5}M_\odot$ to 90% confidence. Immediate release of $\mathcal{M}$ for future sources would preclude the need for speculation, involve wider participation among theorists, and attract more observational resources to aid in the search for EM counterparts.

Further upgrades and observations will result in many more neutron star merger detections. Combined with multimessenger observations, improved constraints on radii and M_{max} seem likely.

If it is confirmed that the Galactic BNS distribution also applies to extra-Galactic sources, the narrow range of observed $\mathcal{M}$ will ease the combining of results and thereby reduce uncertainties in $\tilde{\Lambda}_{\mathcal{M}}$; however, if the two distributions prove to be distinct, a wider range of neutron star masses will be probed. The additional capabilities of next-generation GW detectors may also allow the measurement of dynamical tides, the tidal disruption phase, and postmerger oscillations that could probe internal structure, including possible identification of a quark–hadron phase transition (12, 146).

5. PULSE-PROFILE MODELING

Pulse-profile modeling probes general relativistic effects on thermal emission from hot regions (spots) on the stellar surface of rapidly rotating neutron stars (147). These models include local radiation beaming due to the bulk motion of material on the rotationally deformed surface and the subsequent ray propagation through the exterior space-time. Ray propagation includes gravitational light bending and redshift and rotational effects like frame dragging, a finite-mass quadrupole moment (due to stellar oblateness), and higher-order mass and current multipole moments. The magnetic polar caps of millisecond pulsars, thought to be heated by currents in the pulsar magnetosphere, produce thermal emission in the soft X-ray band (148). As the star spins, the X-ray emission is perceived to be periodically modulated, which allows the construction of X-ray counts in each detector energy channel's rotational phase (pulse profile). The relativistic ray tracing that maps the surface emission into the pulse profile detected by a distant observer has been well studied (149–159). A surface emission model that consists of a thin atmosphere together with an assumed temperature distribution (i.e., the number, shapes, sizes, and temperatures of hot spots) can then be used to compute a light curve. Bayesian inference is used to couple light-curve models to statistical sampling software to derive posterior PDFs for mass and equatorial radius directly from pulse-profile data (160–162). Although the redshift is expected to be the best-determined quantity, oscillation amplitudes vary with X-ray energies in a way that probes another function of M and R orthogonal to redshift.

The NICER telescope was attached to the International Space Station in 2017 with a primary mission to measure neutron star masses and radii to 5% accuracy through phase-resolved spectroscopy (163). Under initial consideration are PSR J0437-4715 [$1.44 \pm 0.07 M_{\odot}$ (164)], PSR J1614-2230 [$1.908 \pm 0.016 M_{\odot}$ (165)], PSR J0740+6620 [$2.08 \pm 0.07 M_{\odot}$ (25)], and PSRs J1231-1411, J2124-3358, and J0030+0451, whose masses are not previously measured. So far, results have been published for PSR J0030+0451 and PSR J0740+6620.

5.1. PSR J0030+0451

Two NICER teams (30, 31) estimated the joint M and equatorial radius R of the millisecond pulsar PSR J0030+0451 using X-ray Timing Instrument (XTI) photon event data curated in Reference 147. Both teams assumed fully ionized nonmagnetic hydrogen atmospheres and a specific parameterization of the uncertainty in the NICER XTI instrument response. The results are conditional upon the analysis models. Reference 30 assumed two disjoint surface hot regions that could be both nonantipodal and nonidentical, each with some local comoving effective temperature field. The restriction to two disjoint hot regions was motivated by the presence of two distinct pulses in the observed pulse profile. Various shapes for the hot regions, including circles, rings (with the centers both concentric and offset), and crescents, filled with material of a single local comoving temperature, were considered. The favored configuration consists of a small hot spot with an angular extent of only a few degrees and a more extended hot crescent, both
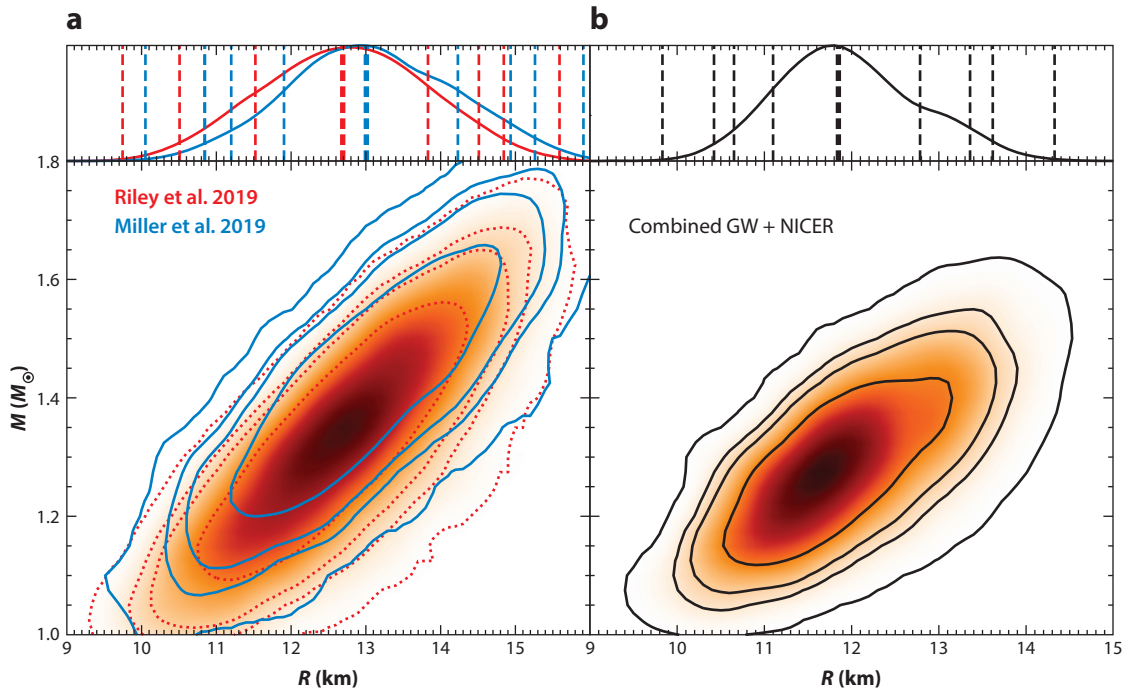
Figure 13

Probability distribution functions in *M-R* space for (*a*) PSR J0030+0451 alone and (*b*) PSR J0030+0451 combined with GW170817. In panel *a*, the filled contours are from Riley et al. (30), and the red-dotted curves indicate enclosed weights of 68.27%, 90%, 95.45%, and 99.73%. The corresponding blue contours are from Miller et al. (31). In panel *b*, the solid contours show the same enclosed weights. The subplots at the top show the marginalized *R* probability densities; bold dashed lines indicate 50%, and light dashed lines indicate the bounds of the same enclosed weights as used for the contour lines. Abbreviations: GW, gravitational wave; NICER, Neutron Star Interior Composition Explorer.

in the same rotational hemisphere. Reference 31 considered models with three and four different uniform-temperature circular hot spots and models with two and three different uniform-temperature oval hot spots, but no evidence was found for different temperatures within a spot or for more than three spots. The spots were allowed to overlap, to have multiple temperatures, and to take a variety of different complex shapes. Models with three different, nonoverlapping, uniform oval spots gave the best fits, although models with two spots were almost as good.

PDFs in *M-R* space, marginalized over other fitting parameters, are shown in **Figure 13*a***. The inferred radius, marginalized over *M*, is $12.72^{+1.14}_{-1.19}$ km in Reference 30 and $13.02^{+1.24}_{-1.06}$ km in Reference 31, but the most accurately determined quantity is the compactness $\beta = GM/(Rc^2)$, which is $0.156^{+0.010}_{-0.008}$ in Reference 30 and $0.163^{+0.008}_{-0.009}$ in Reference 31. From the mean measured differences, one infers a systematic modeling uncertainty in *R* of approximately 0.3 km (2.3%), which is much smaller than the individual uncertainties, and a 0.007 (4.4%) systematic modeling uncertainty in β, which is slightly smaller than the uncertainties in either *M* or *R*. On average, the radius values are about 2 km larger than those inferred from GW170817, yet they comfortably overlap to better than 1σ.

The 1σ mass ranges inferred for the components of GW170817 and PSR J0030+0451 are both approximately 1.1–$1.6 M_\odot$. In this mass interval, $R(M)$ is approximately constant for a given EOS

unless a strong phase transition occurs in that mass interval, corresponding to a density range of 2 to $3.5n_s$. Therefore, it seems reasonable to combine the data from these two independent observations by multiplying their PDFs. Before doing so, however, one can attempt to include the identified systematic modeling uncertainties of the NICER and the GW analyses. For NICER, one can add the PDFs obtained by the two teams (30, 31), and for GW170817, one can add the PDFs obtained by assuming uniform $\sqrt{\Lambda_1 \Lambda_2}$ and uniform R priors. The mean radius becomes $R = 11.85^{+0.94}_{-0.75}$ km (**Figure 13b**). The mean mass is $1.27 M_\odot$, which is about 0.1 km less than for either observation and driven by the large NICER correlation between M and R.

5.2. PSR J0740+6620

NICER also recently released results for radius measurements of the massive pulsar PSR J0740+6620: The Amsterdam team (33) obtained $R = 12.39^{+1.30}_{-0.98}$ km, giving $\Delta R \simeq -0.3^{+1.2}_{-1.5}$ km, while the Maryland team (32) obtained $R = 13.71^{+2.42}_{-1.49}$ km, giving $\Delta R = R_{2.0} - R_{1.4} \simeq 0.7^{+2.9}_{-1.6}$ km. The average value is $\Delta R = 0.2^{+2.2}_{-1.7}$ km.

The inference from Bayesian analysis utilizing parameterized EOSs, constrained by theories of neutron matter, observations of pulsar masses, GWs from mergers, and NICER objects PSR J0030+0451 and PSR J0740+6620, is that $\Delta R \simeq -0.5^{+0.8}_{-1.0}$ km (166) or $\Delta R = 0.0^{+0.5}_{-0.5}$ (32). Both results are averaged over EOS models. These results support the interpretation that $\Delta R \sim 0$, which favors moderate stiffening and disfavors dramatic softening of the EOS at $n_B \gtrsim 2n_s$. Stiffening could result from a first-order phase transition to a phase with sound speed $c_s \gtrsim c/\sqrt{2}$ or a crossover transition to a phase such as quarkyonic matter (83a). Softening would result if a $2M_\odot$ star was a hybrid star with an extensive quark core.

SUMMARY POINTS

1. Advances in many-body theory permit calculations of pure neutron matter (PNM) with quantifiable uncertainties up to nearly twice the nuclear saturation density. These calculations are consistent with the Unitary Gas Conjecture and constraints from nuclear masses, neutron skin thicknesses, nuclear dipole polarizabilities, and the binary neutron star (BNS) merger GW170817. If we assume that the PNM equation of state (EOS) is valid up to $2n_s$, causality constrains $R_{1.4}$ to the interval of 9 to 13 km if $M_{max} \simeq 2M_\odot$ (or 11–13 km for $M_{max} \simeq 2.6M_\odot$). If the PNM EOS is valid and smoothly extrapolated (without a strong phase transition) to $3n_s$, then $R_{1.4} \lesssim 12$ km.

2. PNM and GW170817 radius constraints require that the sound speed above the density $1.5–1.8n_s$ exceed $c/\sqrt{3}$ for $M_{max} \gtrsim 2M_\odot$ or $0.8c$ for $M_{max} \gtrsim 2.6M_\odot$.

3. Parameterized models of the high-density neutron star EOS are powerful tools in inferring bounds for neutron star properties. Semiuniversal relations that relate the stellar binding energy, moment of inertia, tidal polarizability, and fundamental mode oscillation frequency to each other and to M and R have been refined using parameterized EOSs subject to causality and M_{max} constraints.

4. GW170817 observations, coupled with electromagnetic observations of the accompanying short γ-ray burst and kilonova, strongly support $M_{max} \lesssim 2.2–2.3M_\odot$.

5. Evidence strongly suggests a stiffening of the EOS in the range $2–4n_s$. One possibility is the appearance of deconfined quarks with or without a phase transition.

6. Neutron Star Interior Composition Explorer (NICER) pulse-profile constraints of the rapidly rotating pulsars PSR J0030+0451 and PSR J0740+6620 are consistent with expectations from neutron matter theory, nuclear experiments, other observations of quiescent low-mass X-ray binaries, and photospheric radius expansion bursts as well as GW170817. Since the masses of the components of GW170817 and PSR J0030+0451 are nearly the same, their combination leads to improved radius estimates for $1.4 M_\odot$ stars. A slight tension exists between their mean radii, but their differences are within their 1σ uncertainties.

FUTURE ISSUES

1. Further advances in many-body theory for PNM, such as chiral effective field theory studies, may reduce the uncertainties in the dense matter EOS in the important range of 1 to $2n_s$ and, more speculatively, may better constrain the EOS at higher densities.

2. New studies of Δr_{np} in neutron-rich nuclei, both in ^{208}Pb and other nuclei such as ^{48}Ca, will further constrain the symmetry energy density dependence and the parameters S_v and L. In addition, the theoretical estimate for Δr_{np}^{48} depends strongly on $3N$ forces, which can be accessed from both ab initio (few-body) and energy density functional methods.

3. The O3 LIGO/Virgo run yielded as many as three events that may have contained neutron stars, even though none of them may have been a BNS merger. In any case, these events suggest the existence of order $2.5 M_\odot$ compact objects, either very low-mass black holes or very high-mass neutron stars. Either possibility holds important ramifications for $M_{\max}$, stellar evolution, and nucleosynthesis. Additional events will determine whether the extra-Galactic and Galactic distributions of BNS mergers are similar.

4. If the Galactic distribution of BNS masses proves to be typical, the expected mass range of future BNS merger events will be so small that it will be possible to usefully combine observations to enhance the tidal deformability constraints. Moreover, the expectation would be that most BNS mergers are accompanied by short γ-ray bursts, kilonovae, r-process nucleosynthesis, and possibly magnetar heating, leading to additional multimessenger events and constraints for those systems close enough to permit observation.

5. It is imperative that future gravitational wave observatories have greater sensitivity at 1- to 3-kHz frequencies than at present. Not only would this enable more precise tidal deformability measurements, but it would also permit the observation of dynamical tidal resonances during the inspiral phase, the tidal disruption phase, and postmerger oscillation frequencies. Semiuniversal relations can connect such observables with each other and with other neutron star structural properties and could reveal the existence of strong phase transitions.

6. The anticipated measurement of the moment of inertia for PSR J0737-3039A would provide a critical independent determination of the neutron star radius and tidal deformability (via the *I*-Love universal relation) for a precisely known mass, with important implications for the dense matter EOS. Additional neutron star mass measurements will refine our understanding of the BNS mass distribution and the lower limit of $M_{\max}$.

7. Additional NICER observations of massive neutron stars near $2M_\odot$ will probe the neutron star radius in a different domain than previously, increasing our knowledge of the EOS beyond $2n_s$. New generations of X-ray space telescopes, such as the enhanced X-ray Timing and Polarimetry (eXTP) mission (167) and the Advanced Telescope for High Energy Astrophysics (ATHENA) (168), will significantly reduce observational uncertainties from the pulse-profile method for rapidly rotating stars and from observations of quiescent and bursting sources.

DISCLOSURE STATEMENT

ACKNOWLEDGMENTS

LITERATURE CITED

1. Janka H-T. *Annu. Rev. Nucl. Part. Sci.* 62:407 (2012)
2. Burrows A, Lattimer JM. *Astrophys. J.* 307:178 (1986)
3. Hirata K, et al. *Phys. Rev. Lett.* 58:1490 (1987)
4. Bionta RM, et al. *Phys. Rev. Lett.* 58:1494 (1987)
5. Page D, Lattimer JM, Prakash M, Steiner AW. *Astrophys. J. Suppl.* 155:623 (2004)
6. Baym G, Bethe HA, Pethick CJ. *Astrophys. J.* 170:299 (1971)
7. Pethick CJ, Ravenhall DJ, Lorenz CP. *Nucl. Phys. A* 584:675 (1995)
8. Balliet L, Newton W, Canfu S, Budmir S. arXiv:2009.07696 [astro-ph.HE] (2020)
9. Kurkela A, Romatschke P, Vuorinen A. *Phys. Rev. D* 81:105021 (2010)
10. Lattimer JM, Prakash M. *Phys. Rep.* 411:325 (2007)
11. Alford MG, Han S. *Eur. Phys. J. A* 52:62 (2016)
12. Radice D, Bernuzzi S, Perego A. *Annu. Rev. Nucl. Part. Sci.* 70:95 (2020)
13. Tews I, Lattimer JM, Ohnishi A, Kolomeitsev EE. *Astrophys. J.* 848:105 (2017)
14. Heinke CO, Ho WCG. *Astrophys. J. Lett.* 719:L167 (2010)
15. Page D, Prakash M, Lattimer JM, Steiner AW. *Phys. Rev. Lett.* 106:081101 (2011)
16. Yakovlev DG, et al. *Mon. Not. R. Astron. Soc.* 411:1977 (2011)
17. Cigan P, et al. *Astrophys. J.* 886:51 (2019)
18. Page D, et al. *Astrophys. J.* 898:125 (2020)
19. Boguta J. *Phys. Lett. B* 106:255 (1981)
20. Lattimer JM, Pethick CJ, Prakash M, Haensel F. *Phys. Rev. Lett.* 66:2701 (1991)
21. Lattimer JM. *Annu. Rev. Nucl. Part. Sci.* 62:485 (2012)
22. Özel F, Freire P. *Annu. Rev. Astron. Astrophys.* 54:401 (2016)
23. Antoniadis J, et al. *Science* 340:448 (2013)
24. Linares M, Shahbaz T, Casares J. *Astrophys. J.* 859:54 (2018)
25. Fonseca E, et al. arXiv:2104.00880 [astro-ph.HE] (2021)
26. Suleimanov VF, et al. *Mon. Not. R. Astron. Soc.* 466:906 (2016)
27. Nättilä J, et al. *Astron. Astrophys.* 608:A31 (2017)

28. Abbott BP, et al. *Phys. Rev. Lett.* 119:161101 (2017)
29. Margalit B, Metzger BD. *Astrophys. J. Lett.* 850:L19 (2017)
30. Riley TE, et al. *Astrophys. J. Lett.* 887:L21 (2019)
31. Miller MC, et al. *Astrophys. J. Lett.* 887:L24 (2019)
32. Miller MC, et al. arXiv:2105.06979 [astro-ph.HE] (2021)
33. Riley TE, et al. arXiv:2105.06980 [astro-ph.HE] (2021)
34. Bombaci I, Lombardo U. *Phys. Rev. C* 44:1892 (1991)
35. Drischler C, Somá V, Schwenk A. *Phys. Rev. C* 89:025806 (2014)
36. Wellenhofer C, Holt JW, Kaiser N. *Phys. Rev. C* 93:055802 (2016)
37. Weinberg S. *Phys. Rev. Lett.* 18:507 (1967)
38. Weinberg S. *Phys. Rev.* 166:1569 (1968)
39. Epelbaum E, Hammer H-W, Meißner U-G. *Rev. Mod. Phys.* 81:1773 (2009)
40. Machleidt R, Entem D. *Phys. Rep.* 503:1 (2011)
41. Hammer H-W, König S, van Kolck U. *Rev. Mod. Phys.* 92:025004 (2020)
42. Tews I, et al. *J. Phys. G* 47:103001 (2020)
43. Drischler C, Hebeler K, Schwenk A. *Phys. Rev. Lett.* 122:042501 (2019)
44. Leonhardt M, et al. *Phys. Rev. Lett.* 125:142502 (2020)
45. Drischler C, Melendez JA, Furnstahl RJ, Phillips DR. *Phys. Rev. C* 102:054315 (2020)
46. Drischler C, Furnstahl RJ, Melendez JA, Phillips DR. *Phys. Rev. Lett.* 125:202702 (2020)
47. Drischler C, Holt JW, Wellenhofer C. *Annu. Rev. Nucl. Part. Sci.* 71:403 (2021)
48. Brown BA. *Phys. Rev. Lett.* 111:232502 (2013)
49. Zhang Z, Chen L-W. *Phys. Rev. C* 92:031301 (2015)
50. Drischler C, et al. *Phys. Rev. C* 103:045808 (2021)
51. Hebeler K, Schwenk A. *Phys. Rev. C* 82:014314 (2010)
52. Hebeler K, Lattimer JM, Pethick CJ, Schwenk A. *Astrophys. J.* 773:11 (2013)
53. Kortelainen M, et al. *Phys. Rev. C* 82:024313 (2010)
54. Lattimer JM, Steiner AW. *Eur. Phys. J. A* 50:40 (2014)
55. Roca-Maza X, Centelles M, Viñas X, Warda M. *Phys. Rev. Lett.* 106:252501 (2011)
56. Chen L-W, Ko C, Li B-A, Xu J. *Phys. Rev. C* 82:024321 (2010)
57. Tarbert CM, et al. *Phys. Rev. Lett.* 112:242502 (2014)
58. Friedman E. *Nucl. Phys. A* 896:46 (2012)
59. Klos B, et al. *Phys. Rev. C* 76:034305 (2007)
60. Brown BA, et al. *Phys. Rev. C* 76:014311 (2007)
61. Zenhiro J, et al. *Phys. Rev. C* 82:044611 (2010)
62. Pruitt CD, et al. *Phys. Rev. Lett.* 125:102501 (2020)
63. Adhikari D, et al. *Phys. Rev. Lett.* 126:172502 (2021)
64. Abrahamyan S, et al. *Phys. Rev. Lett.* 108:112502 (2012)
65. Reed B, Jaffe Z, Horowitz CJ, Sfienti C. *Phys. Rev. C* 102:064308 (2020)
66. Reed BT, Fattoyev FJ, Horowitz CJ, Piekarewicz J. *Phys. Rev. Lett.* 126:172503 (2021)
67. Horowitz CJ, Kumar KS, Michaels R. *Eur. Phys. J. A* 50:48 (2014)
68. Hagan G, et al. *Nat. Phys.* 12:186 (2016)
69. Roca-Maza X, et al. *Phys. Rev. C* 88:024316 (2013)
70. Tamii A, et al. *Phys. Rev. Lett.* 107:062502 (2012)
71. Trippa L, Coló G, Vigezzi E. *Phys. Rev. C* 77:061304 (2008)
72. Zwierlein MW. Superfluidity in ultracold atomic Fermi gases. In *Novel Superfluids*, Vol. 2, ed. KH Bennemann, JB Ketterson, pp. 269–422. Oxford, UK: Oxford Univ. Press (2015)
73. Ku MJH, Sommer AT, Cheui LW, Zwierlein MW. *Science* 335:563 (2012)
74. Zürn G, et al. *Phys. Rev. Lett.* 110:135301 (2013)
75. Matsuo M. *Phys. Rev. C* 73:044309 (2006)
76. Navon N, Naxcimbéne S, Chevy F, Salomon C. *Science* 328:729 (2010)
77. Koranda S, Stergioulas N, Friedman JL. *Astrophys. J.* 488:799 (1997)
78. Read JS, Lackey BD, Owen BJ, Friedman JL. *Phys. Rev. D* 79:124032 (2009)

79. Lindblom L. *Phys. Rev. D* 82:103011 (2010)
80. Greif SK, et al. *Mon. Not. R. Astron. Soc.* 485:5363 (2019)
81. Annala E, et al. *Nat. Phys.* 16:907 (2020)
82. Todd-Rutel BG, Piekarewicz J. *Phys. Rev. Lett.* 95:122501 (2005)
83. McLerran L, Reddy S. *Phys. Rev. Lett.* 122:122701 (2019)
83a. Zhao T, Lattimer JM. *Phys. Rev. D* 102:023021 (2020)
84. Lattimer JM, Prakash M. *Astrophys. J.* 550:426 (2001)
85. Burrows A, Lattimer JM. *Astrophys. J. Lett.* 318:L63 (1988)
86. Damour T, Schaefer G. *Nuovo Cim. B* 101:127 (1988)
87. Lattimer JM, Shutz BF. *Astrophys. J.* 629:979 (2005)
88. Flanagan EE, Hinderer T. *Phys. Rev. D* 77:021502 (2008)
89. Hinderer T. *Astrophys. J.* 677:1216 (2008)
90. Andersson N, Kojima Y, Kokkotas KD. *Astrophys. J.* 462:855 (1996)
91. Lattimer JM, Yahil A. *Astrophys. J.* 340:426 (1989)
92. Greif SK, et al. *Astrophys. J.* 901:155 (2020)
93. Steiner AW, et al. *Eur. Phys. J. A* 52:2 (2016)
94. Breu C, Rezzolla L. *Mon. Not. R. Astron. Soc.* 459:646 (2016)
95. Yagi K, Yunes N. *Science* 341:365 (2013)
96. Postnikov S, Prakash M, Lattimer JM. *Phys. Rev. D* 82:024016 (2010)
97. Bauswein A, Janka H-T, Hebeler K, Schwenk A. *Phys. Rev. D* 86:063001 (2012)
98. Tsui LK, Leung PT. *Mon. Not. R. Astron. Soc.* 357:1029 (2005)
99. Chan TK, Sham YH, Leung PT, Lin LM. *Phys. Rev. D* 89:124023 (2016)
100. Goldstein A, et al. *Astrophys. J. Lett.* 848:L14 (2017)
101. Savchenko V, et al. *Astrophys. J. Lett.* 848:L15 (2017)
102. Kasliwal MM, et al. *Science* 358:1559 (2017)
103. Paczynski B. *Astrophys. J.* 308:L43 (1986)
104. Metzger BD, et al. *Mon. Not. R. Astron. Soc.* 406:2650 (2010)
105. Lattimer JM, Schramm DN. *Astrophys. J. Lett.* 192:L145 (1974)
106. Hinderer T, Lackey BD, Lang RN, Read JS. *Phys. Rev. D* 81:123016 (2010)
107. Zhao T, Lattimer JM. *Phys. Rev. D* 98:063020 (2018)
108. Fishbone L. *Astrophys. J.* 185:43 (1973)
109. Ackley K, et al. *Publ. Astron. Soc. Aust.* 37:e047 (2020)
110. Sathyaprakash BS, Dhurandhar SV. *Phys. Rev. D* 44:3819 (1991)
111. Buonanno A, et al. *Phys. Rev. D* 80:084043 (2009)
112. De S, et al. *Phys. Rev. Lett.* 121:091102 (2018)
113. Abbott BP, et al. *Phys. Rev. X* 9:011001 (2019)
114. Capano CD, et al. *Nat. Astron.* 4:625 (2020)
115. Bauswein A, Stergioulas N. *Mon. Not. R. Astron. Soc.* 471:4 (2017)
116. Radice D, Perego A, Zappa F, Bernuzzi S. *Astrophys. J. Lett.* 852:L29 (2018)
117. Kiuchi K, Kyutoku K, Shibata M, Taniguchi K. *Astrophys. J. Lett.* 876:L31 (2019)
118. Haensel P, Zdunik JL, Bejger M, Lattimer JM. *Astron. Astrophys.* 502:605 (2009)
119. Radice D, Perego A, Bernuzzi S, Zhang B. *Mon. Not. R. Astron. Soc.* 481:3670 (2018)
120. Lasota J-P, Haensel P, Abramowicz MA. *Astrophys. J.* 456:400 (1996)
121. Ruiz M, Shapiro SL, Tsokaros A. *Phys. Rev. D* 97:021501 (2018)
122. Rezzolla L, Most ER, Weih LR. *Astrophys. J. Lett.* 852:L52 (2018)
123. Shibata M, Zhou E, Kiuchi K, Fujibayashi S. *Phys. Rev. D* 100:023015 (2019)
124. Ai S, Gao H, Zhang B. *Astrophys. J.* 893:2 (2020)
125. Tauris TM, et al. *Astrophys. J.* 846:170 (2017)
126. Fong W, et al. *Astrophys. J.* 906:127 (2021)
127. Masuda K, Hirano T. *Astrophys. J. Lett.* 910:L17 (2021)
128. Jayasinghe T, et al. *Mon. Not. R. Astron. Soc.* 504:2577 (2021)
129. van den Heuvel EPJ, Tauris TM. *Science* 368:eaba3282 (2020)

130. Abbott R, et al. *Phys. Rev. X* 11:021053 (2021)
131. Abbott BP, et al. *Astrophys. J. Lett.* 892:L3 (2020)
132. Abbott BP, et al. *Astrophys. J. Lett.* 896:L2 (2020)
133. Foley RJ, et al. *Mon. Not. R. Astron. Soc.* 494:190 (2020)
134. Han M-Z, et al. *Astrophys. J. Lett.* 891:L5 (2020)
135. Thompson TA, et al. *Science* 366:637 (2019)
136. Tan H, Noronha-Hostler J, Yunes N. *Phys. Rev. Lett.* 125:261104 (2020)
137. Lim Y, Bhattacharya A, Holt JW, Pati D. arXiv:2007.06526 [nucl-th] (2020)
138. Tews I, et al. *Astrophys. J. Lett.* 908:L1 (2021)
139. Essik R, Landry P. *Astrophys. J.* 904:80 (2020)
140. Tsokaros A, Ruiz M, Shapiro SL. *Astrophys. J.* 905:48 (2020)
141. Fattoyev F, Horowitz C, Piekarewicz J, Reed B. *Phys. Rev. C* 102:065805 (2020)
142. Godzieba DA, Radice D, Bernuzzi S. *Astrophys. J.* 908:122 (2021)
143. Kanakis-Pegios A, Koliogiannis P, Moustakidis C. *Phys. Rev. C* 102:055801 (2020)
144. LIGO/Virgo Collab. GCN Circular 24168 (2019); LIGO/Virgo Collab. GCN Circular 24411 (2019)
145. Lattimer JM. arXiv:1908.03622 [astro-ph.HE] (2019)
146. Pratten G, Schmidt P, Hinderer T. *Nat. Commun.* 11:2553 (2020)
147. Bogdanov S, et al. *Astrophys. J. Lett.* 887:L25 (2019)
148. Harding AK, Muslimov AG. *Astrophys. J.* 568:862 (2002)
149. Pechenick KR, Ftaclas C, Cohen JM. *Astrophys. J.* 274:846 (1983)
150. Miller MC, Lamb FK. *Astrophys. J.* 808:31 (2015)
151. Poutanen J, Gierliński M. *Mon. Not. R. Astron. Soc.* 343:1301 (2003)
152. Poutanen J, Belobrodov AM. *Mon. Not. R. Astron. Soc.* 373:836 (2006)
153. Cadeau C, Morsink SM, Leahy D, Campbell SS. *Astrophys. J.* 654:415 (2007)
154. Morsink SM, Leahy DA, Cadeau C, Braga J. *Astrophys. J.* 663:1244 (2007)
155. Bauböck M, Berti E, Psaltis D, Özel F. *Astrophys. J.* 777:68 (2013)
156. AlGendy M, Morsink SM. *Astrophys. J.* 791:78 (2014)
157. Psaltis D, Özel F. *Astrophys. J.* 792:87 (2014)
158. Nättilä J, Pihajoki P. *Astron. Astrophys.* 615:A50 (2018)
159. Vincent FH, et al. *Astrophys. J.* 855:116 (2018)
160. Bogdanov S, Heinke CO, Özel F, Güver T. *Astrophys. J.* 831:184 (2016)
161. Watts AL, et al. *Rev. Mod. Phys.* 88:021001 (2016)
162. Watts AL. *AIP Conf. Proc.* 2127:020008 (2019); Watts AL. arxiv:1904.07012 [astro-ph.HE] (2019)
163. Gendreau KC, et al. *Proc. SPIE* 9905:99051H (2016)
164. Reardon DJ, et al. *Mon. Not. R. Astron. Soc.* 478:1093 (2016)
165. Arzoumanian Z, et al. *Astrophys. J. Suppl.* 235:37 (2018)
166. Raaijmakers G, et al. arXiv:2105.06981 [astro-ph.HE] (2021)
167. Zhang SN, et al. *Sci. China Phys. Mech. Astron.* 62:29502 (2019)
168. Barret D, et al. *Astron. Nachr.* 341:224 (2020)

Erratum >